

## Excitons and plasmons of graphene nanoribbons in infrared frequencies in an effective-mass approximation

Seiji Uryu <sup>\*</sup>*Department of Physical Science and Materials Engineering, Iwate University, 4-3-5 Ueda, Morioka, Iwate 020-8551, Japan*

(Received 9 August 2020; accepted 21 September 2020; published 9 October 2020)

Effects of electron-electron interactions on the optical response of graphene nanoribbons are theoretically investigated in an effective-mass approximation in a comprehensive manner. In optical absorption spectra of armchair and zigzag nanoribbons without and with doping, excitons, which are bound states of electrons and holes, and plasmons manifest themselves as various prominent peaks. For light polarized parallel to nanoribbons, exciton peaks at high energies split because of interactions with dark excitons, to which optical transition is prohibited. For light polarized perpendicular to nanoribbons, in nondoped semiconducting armchair nanoribbons, moderate exciton peaks appear while in doped armchair and zigzag nanoribbons, only when the Fermi energy crosses at least two energy bands, large plasmon peaks occur because of a nature of Dirac electrons. These peaks can be assigned to specific optical transitions in energy bands. The optical absorption peaks arising from the excitons and plasmons in a wide range of categories of nanoribbons approximately correspond to those of carbon nanotubes by appropriate scaling of energy and the wave vector.

DOI: [10.1103/PhysRevB.102.155409](https://doi.org/10.1103/PhysRevB.102.155409)

### I. INTRODUCTION

Graphene nanoribbons are strips of graphene, which is a single layer of a carbon honeycomb lattice. Among various graphene nanoribbons, representative structures are armchair nanoribbons and zigzag nanoribbons. Electronic structure of graphene nanoribbons has been intensively investigated in many theoretical studies. Fujita *et al.* showed that armchair nanoribbons are metal or semiconductor depending on the width while zigzag nanoribbons are metal where edge states, which are states localized near edges, exist at the Fermi energy and cause spin polarization [1–4]. This is partially modified in first-principles calculations by Son *et al.* to that all armchair and zigzag nanoribbons have energy gaps [5,6]. A method to detect electronic structure of systems is to measure their optical response. In low-dimensional systems, electron-electron interactions can play important roles. In carbon nanotubes, for example, prominent effects of excitons [7–15], which are bound states of photoexcited pairs of an electron and a hole, and plasmons can appear [16–28]. Therefore, understanding of electron-electron interactions in graphene nanoribbons is necessary for study of their electronic structure and also for their applications. The purpose of this paper is to theoretically clarify effects of electron-electron interactions on optical absorption of graphene nanoribbons in a comprehensive manner.

In optical absorption spectra of graphene nanoribbons in one-particle models, peaks appear because of van Hove singularities of the joint density of states [29–38]. Some of these peaks change to steep exciton peaks by including attractive interactions between electrons and holes [39–45]. It was shown in first-principles calculations by Yang *et al.* [39,40] and

Prezzi *et al.* [41] that in narrow armchair and zigzag nanoribbons with widths of about one nanometer, excitons exist with large binding energies of several hundreds of millielectron volts to one electron volt. In wider armchair nanoribbons with widths of up to about three nanometers, family patterns of exciton energy as a function of the width were reported in a theoretical study [42]. Excitons in narrow nanoribbons were experimentally observed [46,47]. These studies mainly focused on the lowest and second lowest excitons in energy.

Plasmons in metallic and doped graphene nanoribbons have been reported in many theoretical studies [48–53]. It was shown that the excitation energy of plasmons in metallic and doped nanoribbons vanishes in the long-wavelength limit as  $k\sqrt{-\log(kW)}$  with  $k$  being the wave vector along nanoribbons and  $W$  being the width, which is characteristic of one-dimensional systems [48,52]. Because of the vanishing energy of the plasmons in the long-wavelength limit, other plasmons are often used in experiments for applications in spectroscopy and sensing [54–56], which are polarized across nanoribbons with finite excitation energies. These plasmons have also been theoretically studied [50,57]. Most of these studies do not fully consider the quantum-mechanical nature of Dirac electrons in nanoribbons partially because wide nanoribbons are considered, where classical electromagnetic description works well. However, full quantum-mechanical calculations of these plasmons would be necessary as clarified in the case of carbon nanotubes [58–62].

Graphene nanoribbons have often been compared to carbon nanotubes because of their similarity in atomic structure [31,36–38,63]. In theoretical studies, correspondence of energy bands and optical absorption spectra of armchair (zigzag) nanoribbons with those of zigzag (armchair) nanotubes was reported [36–38]. Although one-to-one correspondence was shown in these studies, such correspondence is expected to

<sup>\*</sup>uryu@iwate-u.ac.jp

expand in a wider range of categories of nanoribbons and nanotubes because energy bands of nanoribbons and nanotubes are scaled by the width and the circumference length, respectively, near the Fermi energy [64,65]. Additionally, effects of excitons and plasmons on the correspondence need to be investigated, which were not considered in the earlier studies. Difference between nanoribbons and nanotubes should also be noted. The width of nanoribbons can become much wider than the diameter of single-wall nanotubes, where the former ranges from a subnanometer scale to several hundreds of nanometers [46,66–75] while the latter is typically of the order of one nanometer [76–86]. This leads to that for nanoribbons, energies of excitons and plasmons which are scaled by the width can be lowered in infrared frequencies as compared to those for nanotubes, which are typically in near infrared and visible frequencies. In this case, phenomena associated with high conduction and low valence bands may be important in nanoribbons.

In this paper, we theoretically study optical absorption of graphene nanoribbons with electron correlations in an effective-mass approximation. In calculated optical absorption spectra, various prominent peaks are assigned to various excitons and plasmons, where plasmons polarized across nanoribbons show characteristic dependence on the Fermi energy because of a nature of Dirac electrons. Most of these peaks approximately correspond to those of carbon nanotubes. However, some exciton peaks at high energies exhibit a character different from those of nanotubes. The correspondence exists in a much wider range of categories of nanoribbons and nanotubes as compared to that reported in the earlier studies.

The paper is organized as follows: In Sec. II, our model and method are described. An effective-mass approximation for armchair and zigzag graphene nanoribbons is reformulated and the random-phase approximation (RPA) describing excited states with electron correlations is introduced. Optical absorption spectra with depolarization effects are formulated for nanoribbons and an optical selection rule is reviewed. In Sec. III, numerical results of screened Coulomb interactions and optical absorption spectra of armchair and zigzag nanoribbons without and with doping are presented. In Sec. IV, comparison of optical absorption spectra of graphene nanoribbons with those of carbon nanotubes is made and methods to calculate optical absorption spectra including depolarization effects are discussed. A brief summary and conclusions are given in Sec. V.

## II. MODEL AND METHOD

### A. Graphene in an effective-mass approximation

One-particle states of graphene nanoribbons in an effective-mass approximation were reported in a previous study [64]. However, we derive a similar formulation again in Secs. II A–II C because it is necessary for formulation for graphene nanoribbons with electron correlations and because it makes correspondence between graphene nanoribbons and carbon nanotubes even clearer.

In an effective-mass approximation, wave functions of electrons in the  $\pi$  bands of graphene are expanded near the

Fermi energy by those at two valleys, i.e., the  $K$  and  $K'$  points, which are written as [65,87]

$$\psi_A(\mathbf{r}) = F_A^K(\mathbf{r})e^{i\mathbf{K}\cdot\mathbf{r}} + F_A^{K'}(\mathbf{r})e^{i\mathbf{K}'\cdot\mathbf{r}}, \quad (1)$$

$$\psi_B(\mathbf{r}) = -\omega F_B^K(\mathbf{r})e^{i\mathbf{K}\cdot\mathbf{r}} + F_B^{K'}(\mathbf{r})e^{i\mathbf{K}'\cdot\mathbf{r}}, \quad (2)$$

where  $\omega = e^{2\pi i/3}$ , A and B denote sublattices,  $\mathbf{K} = (2\pi/a)(1/3, 1/\sqrt{3})$  and  $\mathbf{K}' = (2\pi/a)(2/3, 0)$  with  $a = 2.46 \text{ \AA}$  being the lattice constant are wave vectors for the  $K$  and  $K'$  points, respectively, and  $F_\alpha^v(\mathbf{r})$  is an envelope function for a valley  $v = \{K, K'\}$  and a sublattice  $\alpha = \{A, B\}$ , which slowly varies as a function of position  $\mathbf{r} = (x, y)$  in comparison with the lattice constant. An equation of motion for  $\mathbf{F}^v(\mathbf{r}) = (F_A^v(\mathbf{r}), F_B^v(\mathbf{r}))^T$  is given by  $H^v\mathbf{F}^v(\mathbf{r}) = \varepsilon^v\mathbf{F}^v(\mathbf{r})$  with  $H^v$  and  $\varepsilon^v$  being a Hamiltonian and an eigenenergy, respectively, for a valley  $v$ . For the  $K$  point, we have [65,87,88]

$$H^K = \gamma(\hat{k}_x\sigma_x + \hat{k}_y\sigma_y), \quad (3)$$

where  $\gamma$  is a band parameter,  $\hat{k}_\mu = -i\partial/\partial\mu$  with  $\mu = \{x, y\}$  is a wave vector operator,  $\sigma_\mu$  denotes the Pauli spin matrix, and the Fermi energy is chosen as the origin of energy. For the  $K'$  point,  $H^{K'}$  is given by  $H^{K*}$ .

Eigenenergies are given by  $\varepsilon^v = s_e\gamma|\mathbf{k}|$ , where  $s_e$  is 1 and  $-1$  for the conduction and valence bands, respectively, and  $\mathbf{k} = (k_x, k_y)$  is a wave vector. Envelope functions are given by  $F_\alpha^v(\mathbf{r}) = F_{\alpha,t}e^{i\mathbf{k}\cdot\mathbf{r}}/\sqrt{AW}$  with  $A$  and  $W$  being the length and width of the system and [65,87]

$$\begin{pmatrix} F_{A,t} \\ F_{B,t} \end{pmatrix} = \frac{1}{\sqrt{2}} \begin{pmatrix} e^{\mp i\varphi} \\ s_e \end{pmatrix}, \quad (4)$$

where  $t$  denotes a set of parameters  $(v, s_e, \mathbf{k})$  and  $e^{\mp i\varphi} = (k_x \mp ik_y)/|\mathbf{k}|$  for the  $K$  ( $-$ ) and  $K'$  ( $+$ ) points.

For zigzag edges, edge states, which are evanescent waves localized near edges, can be solutions. In the case of zigzag edges along the  $x$  direction, for example, eigenenergies and envelope functions for the  $K$  point are given by  $\varepsilon^K = s_e\gamma\sqrt{k_x^2 - \tilde{k}_y^2}$  and  $F_\alpha^K(\mathbf{r}) = \tilde{F}_{\alpha,t}e^{ik_x x \mp \tilde{k}_y y}$  ( $\tilde{k}_y > 0$ ), respectively, where  $\tilde{k}_y$  is the inverse of decay length and

$$\begin{pmatrix} \tilde{F}_{A,t} \\ \tilde{F}_{B,t} \end{pmatrix} = \begin{pmatrix} k_x \pm \tilde{k}_y \\ \sqrt{k_x^2 - \tilde{k}_y^2} \\ s_e \end{pmatrix}, \quad (5)$$

with  $t = (K, s_e, (k_x, \tilde{k}_y))$ . Equation (5) is not normalized for convenience. In  $F_\alpha^K(\mathbf{r})$  and Eq. (5),  $\pm$  are chosen in such a way that the envelope functions decay as the distance from the edge increases. For the  $K'$  point, eigenenergies are the same as those for the  $K$  point and envelope functions are given by Eq. (5) with  $\tilde{k}_y \rightarrow -\tilde{k}_y$ .

### B. Armchair nanoribbons

Armchair nanoribbons are shown in Fig. 1(a), where armchair shaped edges are along the  $y$  direction and a number  $N$  specifies the width of the nanoribbons. When the  $x$  coordinate of the left edge is chosen as zero, A and B sites at the left edge are, respectively, located at

$$\mathbf{R}_A^e = n_x\mathbf{a} + n_y(\mathbf{a} + 2\mathbf{b}) + \boldsymbol{\tau}_1, \quad \mathbf{R}_B^e = \mathbf{R}_A^e - \boldsymbol{\tau}_1, \quad (6)$$

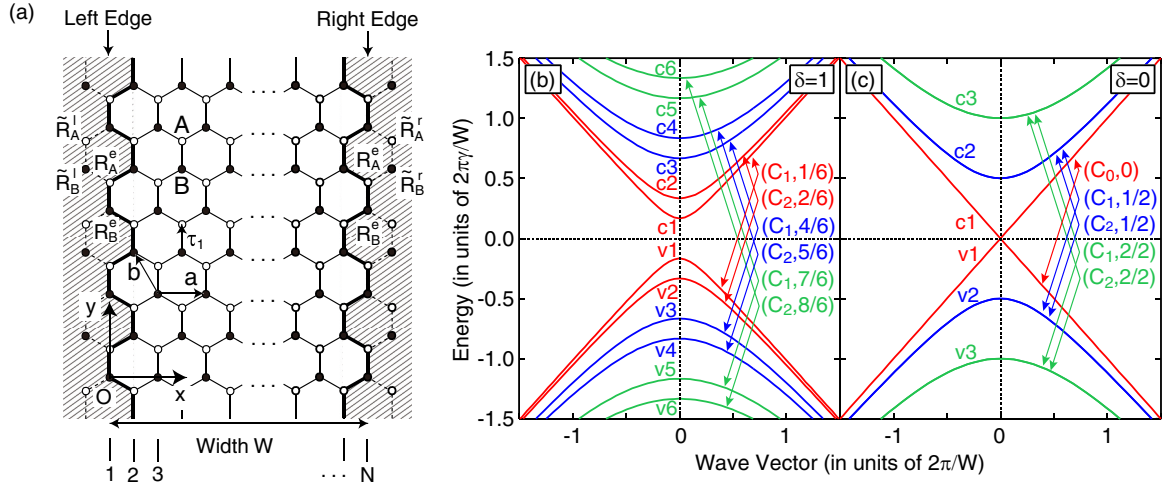


FIG. 1. (a) Schematic illustration of armchair graphene nanoribbons. Open and closed circles denote sites of A and B sublattices, respectively. Positions of edges are located at  $\tilde{\mathbf{R}}_\alpha^e$  with  $\alpha = \{A, B\}$  and  $\tilde{\mathbf{R}}_\alpha^l$  and  $\tilde{\mathbf{R}}_\alpha^r$  denote sites where a boundary condition is imposed. The origin of the coordinate system is set to a B site at the left edge. A number  $N$  specifies the width of the nanoribbons. (b) and (c) Energy bands of (a) semiconducting ( $\delta = 1$ ) and (b) metallic ( $\delta = 0$ ) armchair nanoribbons. Indices  $vi$  and  $ci$  with  $i$  being integers are those for the valence and conduction bands, respectively. On the positive side of the wave vector,  $\mathbf{C}_i$  with  $i = \{0, 1, 2\}$  in Eqs. (12) and (14) and the wave vectors across the nanoribbons in units of  $2\pi/W$  are assigned to the energy bands.

with  $\mathbf{a}$  and  $\mathbf{b}$  being primitive lattice vectors,  $\boldsymbol{\tau}_1$  being a vector connecting A and B sites neighboring in the  $y$  direction,  $n_x = 0$ , and  $n_y$  being integers. Positions of A and B sites at the right edge are given by Eq. (6) with  $n_x = (N - 1)/2$  for odd  $N$  and by  $\tilde{\mathbf{R}}_\alpha^e + \mathbf{a} + \mathbf{b}$  with  $n_x = (N - 2)/2$  for even  $N$ .

As a boundary condition, we impose that the wave functions in Eqs. (1) and (2) vanish at sites outside the edges which are located at  $\tilde{\mathbf{R}}_\alpha^l$  and  $\tilde{\mathbf{R}}_\alpha^r$  in Fig. 1(a) for the left and right edges, respectively. The  $y$  coordinates of  $\tilde{\mathbf{R}}_\alpha^r$  for odd  $N$  are different from those for even  $N$ . The boundary condition leads to that for the envelope functions given by [89]

$$\omega^{p_\beta} F_A^K(\tilde{\mathbf{R}}_A^\beta) + \omega^{p'_\beta} F_A^{K'}(\tilde{\mathbf{R}}_A^\beta) = 0, \quad (7)$$

$$-\omega^{p_\beta} F_B^K(\tilde{\mathbf{R}}_B^\beta) + \omega^{p'_\beta} F_B^{K'}(\tilde{\mathbf{R}}_B^\beta) = 0, \quad (8)$$

where  $\beta = \{r, l\}$  indicates the right ( $r$ ) and left ( $l$ ) edges and  $p_\beta$  and  $p'_\beta$  are defined as

$$\begin{aligned} p_l &= 2, & p'_l &= -1 \\ p_r &= \frac{N}{2} - \frac{1}{2}, & p'_r &= -\frac{N}{2} + \frac{3}{2} \quad \text{for odd } N \\ p_r &= \frac{N}{2} - 2, & p'_r &= -\frac{N}{2} \quad \text{for even } N. \end{aligned} \quad (9)$$

States at the  $K$  and  $K'$  points are mixed by the boundary condition.

Because of the continuous translational symmetry in the direction of nanoribbons, the envelope functions satisfying the boundary condition are written as  $F_\alpha^v(\mathbf{r}) = F_{\alpha,t}(x)e^{ik_y y}/\sqrt{A}$  with  $t = (v, s_e, (k_x, k_y))$ . We assume that for an energy given by  $\varepsilon = s_e \gamma |\mathbf{k}|$ ,  $F_{\alpha,t}(x)$  is expanded for  $k_x \neq 0$  by two plane waves with  $\pm k_x$  ( $k_x > 0$ ) as

$$F_{\alpha,t}(x) = C_+^v F_{\alpha,t+} e^{ik_x x} + C_-^v F_{\alpha,t-} e^{-ik_x x}, \quad (10)$$

with  $C_\pm^v$  being expansion coefficients for a valley  $v$  and  $t_\pm = (v, s_e, (\pm k_x, k_y))$ . Substituting Eq. (10) into Eqs. (7) and (8),

a condition for the existence of nontrivial solutions leads to  $k_x$  given by

$$k_{x,\pm} = \frac{\pi}{W} \left( m \pm \frac{\delta}{3} \right), \quad (11)$$

where  $\delta = p'_r - p_r - p'_l + p_l \bmod 3$  and  $m$  denotes integers satisfying  $k_{x,\pm} > 0$ . Thus the solutions are classified into three cases:  $\delta = 0$  and  $\pm 1$ . From Eq. (9), we have  $\delta = 2 - N \bmod 3$  for both even and odd  $N$ . Thus  $\delta = -1$  and  $1$  for  $N \bmod 3 = 0$  and  $1$ , respectively, and  $\delta = 0$  for  $N \bmod 3 = -1$ .

For  $\delta = 1$ , we have  $\mathbf{C} = (C_+^K, C_-^K, C_+^{K'}, C_-^{K'})^T = \mathbf{C}_1$  for  $k_{x,+}$  and  $\mathbf{C}_2$  for  $k_{x,-}$ , where

$$\mathbf{C}_1 = \frac{1}{\sqrt{2W}} \begin{pmatrix} 1 \\ 0 \\ 0 \\ 1 \end{pmatrix}, \quad \mathbf{C}_2 = \frac{1}{\sqrt{2W}} \begin{pmatrix} 0 \\ 1 \\ 1 \\ 0 \end{pmatrix}. \quad (12)$$

For  $\delta = -1$ , we have  $\mathbf{C} = \mathbf{C}_2$  for  $k_{x,+}$  and  $\mathbf{C}_1$  for  $k_{x,-}$ . For  $\delta = 0$ , energy bands are doubly degenerate. Although eigenfunctions are not uniquely determined in this case, we may choose two solutions as  $\mathbf{C} = \mathbf{C}_1$  and  $\mathbf{C}_2$ , which correspond to those for  $\delta = \pm 1$ .

For  $k_x = 0$ , since there is a single state at each valley,  $F_{\alpha,t}(x)$  is written as

$$F_{\alpha,t}(x) = C^v F_{\alpha,t}, \quad (13)$$

where  $C^v$  is a coefficient for a valley  $v$  and  $t = (v, s_e, (0, k_y))$ . A nontrivial solution  $(C^K, C^{K'})^T = \mathbf{C}_0$  exists only for  $\delta = 0$ , which is given by

$$\mathbf{C}_0 = \frac{1}{\sqrt{2W}} \begin{pmatrix} 1 \\ 1 \end{pmatrix}. \quad (14)$$

Since eigenenergies are given by  $\varepsilon = s_e \gamma |\mathbf{k}|$ , armchair nanoribbons with  $\delta = 0$  are metallic, where linear energy bands with  $k_x = 0$  cross at  $k_y = 0$  and the Fermi energy, and

the others with  $\delta = \pm 1$  are semiconducting. As shown in the above, armchair nanoribbons have a single valley.

Figures 1(b) and 1(c) show energy bands of semiconducting armchair nanoribbons with  $\delta = 1$  and those of metallic ones with  $\delta = 0$ , respectively. Indices  $vi$  and  $ci$  with  $i$  being positive integers are given for the valence and conduction bands, respectively, for later use. On the positive side of the wave vector, the expansion coefficients in Eqs. (12) and (14) and  $k_{x,\pm}$  in units of  $2\pi/W$  are assigned to the energy bands. In Fig. 1(c), the energy bands are doubly degenerate except for the linear dispersions.

Energy bands of carbon nanotubes in an effective-mass approximation are given by  $\varepsilon^v = s_e \gamma \sqrt{\kappa_v(n)^2 + k^2}$ , where  $\kappa_v(n)$  and  $k$  are the components of the wave vector along the circumference and nanotubes, respectively [65]. The component  $\kappa_v(n)$  is given by

$$\kappa_v(n) = \frac{2\pi}{L} \left( n \mp \frac{\nu}{3} \right), \quad (15)$$

where  $L$  is the circumference length,  $n$  indicates integers,  $-$  and  $+$  correspond to the  $K$  and  $K'$  points, respectively, and  $\nu$  is 1 or  $-1$  for semiconducting nanotubes and 0 for metallic ones. Comparing Eq. (11) with Eq. (15), energy bands of armchair nanoribbons are the same as those of carbon nanotubes when energy is scaled by  $\pi\gamma/W$  and  $2\pi\gamma/L$  for nanoribbons and nanotubes, respectively, the wave vector is scaled by  $\pi/W$  and  $2\pi/L$  for nanoribbons and nanotubes, respectively, and  $|\delta| = |\nu|$ , except that nanoribbons have a single valley while nanotubes have two valleys of the  $K$  and  $K'$  points. This suggests that optical absorption spectra of armchair nanoribbons are closely related to those of nanotubes with the corresponding energy bands. The relation is discussed in Sec. IV.

### C. Zigzag nanoribbons

Zigzag nanoribbons in the  $x$  direction are shown in Fig. 2, where  $N$  specifies the width of the nanoribbons. Sites at the lower and higher edges belong to different sublattices, which are located at  $\mathbf{R}_A^e$  and  $\mathbf{R}_B^e$ , respectively. A boundary condition is given as vanishing wave functions at sites outside the edges at  $\tilde{\mathbf{R}}_B = \mathbf{R}_A^e - \boldsymbol{\tau}_1$  and  $\tilde{\mathbf{R}}_A = \mathbf{R}_B^e + \boldsymbol{\tau}_1$ . This leads to a boundary condition for the envelope functions given by [89]

$$F_\alpha^v(\tilde{\mathbf{R}}_\alpha) = 0. \quad (16)$$

In contrast to armchair nanoribbons, states at the  $K$  and  $K'$  points are not mixed by the boundary condition.

The envelope functions are written as  $F_\alpha^v(\mathbf{r}) = F_{\alpha,t}(y)e^{ik_x x}/\sqrt{A}$ , where  $t = (v, s_e, (k_x, k_y))$ . In a similar way to the case of armchair nanoribbons,  $F_{\alpha,t}(y)$  for  $k_y \neq 0$  is expanded as

$$F_{\alpha,t}(y) = D_+^v F_{\alpha,t+} e^{ik_y y} + D_-^v F_{\alpha,t-} e^{-ik_y y}, \quad (17)$$

where  $D_\pm^v$  are expansion coefficients for a valley  $v$ ,  $k_y > 0$ , and  $t_\pm = (v, s_e, (k_x, \pm k_y))$ . A condition of the existence of nontrivial solutions to the boundary condition in Eq. (16) leads to relations between  $k_x$  and  $k_y$  given by

$$\begin{aligned} k_x \sin(k_y W) - k_y \cos(k_y W) &= 0 \quad \text{for the } K \text{ point} \\ k_x \sin(k_y W) + k_y \cos(k_y W) &= 0 \quad \text{for the } K' \text{ point,} \end{aligned} \quad (18)$$

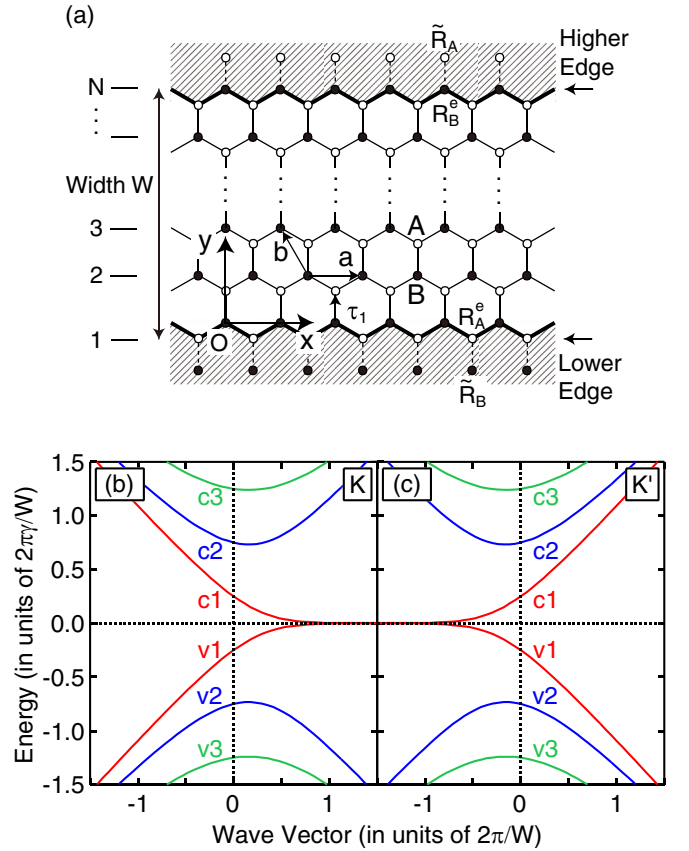


FIG. 2. (a) Schematic illustration of zigzag nanoribbons plotted in a similar way to Fig. 1(a). (b) and (c) Energy bands of zigzag nanoribbons at (a) the  $K$  point and (b) the  $K'$  point. Band indices are given to the energy bands in a similar way to those in Figs. 1(b) and 1(c).

and the coefficients given by

$$\begin{pmatrix} D_+^{K'} \\ D_-^{K'} \end{pmatrix} = \begin{pmatrix} D_+^K \\ D_-^K \end{pmatrix} = C_z \begin{pmatrix} 1 \\ -1 \end{pmatrix}, \quad (19)$$

where  $C_z$  is a normalization factor and its explicit expression is omitted for simplicity. Zigzag nanoribbons have the two valleys. At each valley, eigenenergies are given by  $\varepsilon^v = s_e \gamma |\mathbf{k}|$ . Although the notation of  $F_{\alpha,t}(y)$  in Eq. (17) is the same as that of  $F_{\alpha,t}(x)$  in Eqs. (10) and (13) except for the arguments, the two functions are differently defined, which we distinguish by the arguments for simplicity. When  $k_y = 0$ ,  $F_{\alpha,t}(y)$  is a constant at each valley and the boundary condition cannot be satisfied.

For edge states, the envelope functions are given by  $\tilde{F}_\alpha^v(\mathbf{r}) = \tilde{F}_{\alpha,t}(y)e^{ik_x x}/\sqrt{A}$ , where  $t = (v, s_e, (k_x, \tilde{k}_y))$  with  $\tilde{k}_y > 0$  and

$$\tilde{F}_{\alpha,t}(y) = \tilde{D}_+^v \tilde{F}_{\alpha,t+} e^{-\tilde{k}_y y} + \tilde{D}_-^v \tilde{F}_{\alpha,t-} e^{\tilde{k}_y y}, \quad (20)$$

with  $\tilde{D}_\pm^v$  being expansion coefficients for a valley  $v$  and  $t_\pm = (v, s_e, (k_x, \mp \tilde{k}_y))$ . A similar calculation to the above leads to relations between  $k_x$  and  $\tilde{k}_y$  given by

$$\begin{aligned} k_x \sinh(\tilde{k}_y W) - \tilde{k}_y \cosh(\tilde{k}_y W) &= 0 \quad \text{for the } K \text{ point} \\ k_x \sinh(\tilde{k}_y W) + \tilde{k}_y \cosh(\tilde{k}_y W) &= 0 \quad \text{for the } K' \text{ point.} \end{aligned} \quad (21)$$

Eigenenergies are given by  $\varepsilon^v = s_e \gamma \sqrt{k_x^2 - \tilde{k}_y^2}$  and  $\tilde{D}_\pm^v$  are given by  $D_\pm^v$  in Eq. (19) except for the normalization factor.

Energy bands of zigzag nanoribbons at the  $K$  and  $K'$  points are shown in Figs. 2(b) and 2(c), respectively. Band indices are given in a similar way to those of armchair nanoribbons. Flat parts of the energy bands  $v1$  and  $c1$  at  $\varepsilon^v = 0$  and those close to them correspond to edge states, which are continuously connected to the other parts of the same energy bands for extended states. From Eq. (18), we can easily obtain that tops and bottoms of the valence and conduction bands, respectively, are located at  $k_x \approx 0$  for large  $k_y$ , which is approximately given by  $k_y \approx n\pi/W$  with  $n$  being integers much larger than unity. Thus the energy bands of zigzag nanoribbons at high and low energies are similar to those of metallic armchair nanoribbons and metallic carbon nanotubes.

#### D. Coulomb interactions

In the following, we introduce a notation  $w$  for position along the width of nanoribbons, i.e.,  $w = x$  and  $y$  for armchair and zigzag nanoribbons, respectively, where  $0 \leq w \leq W$ . Since the component of the wave vector along nanoribbons is a good quantum number, Fourier transforms with respect to position along nanoribbons are used. We define the Fourier transform  $f_k$  for a function  $f(x)$  with  $x$  being position along nanoribbons as  $f(x) = (1/A) \sum_k f_k e^{ikx}$  with  $k$  being the wave vector. A Coulomb potential  $V(w, w'; k)$  screened by electrons in nanoribbons is related to the bare Coulomb potential  $V_0(w, w'; k)$  through [90]

$$V_0(w, w'; k) = \int_0^W dw'' \varepsilon(w, w''; k) V(w'', w'; k), \quad (22)$$

where  $\varepsilon(w, w'; k)$  is the dielectric function and

$$V_0(w, w'; k) = \frac{2e^2}{\kappa} K_0(k|w - w'|), \quad (23)$$

with  $\kappa$  being a dielectric constant of the background and  $K_0(z)$  being the modified Bessel function of the second kind of zeroth order. The dielectric function is given in the self-consistent field method by

$$\varepsilon(w, w'; k) = \delta(w - w') + 4\pi \chi(w, w'; k), \quad (24)$$

with  $\chi(w, w'; k)$  being the electric susceptibility given by

$$\begin{aligned} \chi(w, w'; k) &= \frac{e^2 g_s}{2\pi \kappa A} \sum_r \sum_t \delta_{k_r - k_t, k} \\ &\times \frac{f_r - f_t}{\hbar \tilde{\omega} - \varepsilon_t + \varepsilon_r} \int_0^W dw'' K_0(k|w - w''|) \\ &\times [\mathbf{F}_r^\dagger(w'') \mathbf{F}_t(w'')][\mathbf{F}_t^\dagger(w') \mathbf{F}_r(w')], \quad (25) \end{aligned}$$

where  $g_s = 2$  is the spin degeneracy,  $\tilde{\omega}$  is a frequency,  $r$  and  $t$  denote one-particle states, and for a state  $r$ ,  $\varepsilon_r$  is an energy,  $v_r$  denotes a valley,  $k_r$  is a wave vector along nanoribbons,  $f_r$  denotes the Fermi distribution function for  $\varepsilon_r$ , and  $\mathbf{F}_r(w) = (\tilde{F}_{A,r}(w), \tilde{F}_{B,r}(w))^T$  for edge states of zigzag nanoribbons and  $(F_{A,r}(w), F_{B,r}(w))^T$  otherwise. The electric susceptibility is real. In Eq. (25), since our model describes states in the  $\pi$  bands, the summations run over states of which the absolute values of energies are less than half the  $\pi$  band width, and for

zigzag nanoribbons, the valleys for  $r$  and  $t$  must be the same because the long-range Coulomb interactions are considered. In numerical calculations of the screened Coulomb potential, we approximately use the static dielectric function with  $\tilde{\omega} = 0$  at zero temperature, which can reasonably describe effects of the interactions in carbon nanotubes [7,91–95].

Matrix elements of the Coulomb interactions between initial one-particle states  $t$  and  $u$  and final ones  $r$  and  $s$  are given by

$$\begin{aligned} v_{(r;t)(s;u)} &= \frac{1}{A} \delta_{k_r+k_s, k_t+k_u} \int_0^W dw' \int_0^W dw'' V(w', w''; k_r - k_t) \\ &\times [\mathbf{F}_r^\dagger(w') \mathbf{F}_t(w')][\mathbf{F}_s^\dagger(w'') \mathbf{F}_u(w'')], \quad (26) \end{aligned}$$

where for zigzag nanoribbons, the valley of  $r$  ( $s$ ) must be the same as that of  $t$  ( $u$ ). We also define matrix elements of the bare Coulomb interactions  $v_{0,(r;t)(s;u)}$  by  $v_{(r;t)(s;u)}$  where  $V(w', w''; k_r - k_t)$  is replaced by  $V_0(w', w''; k_r - k_t)$ .

The strength of the Coulomb interactions is indicated by  $\kappa$ , for which we use a dimensionless parameter  $(e^2/\kappa W)(2\pi\gamma/W)^{-1} = e^2/2\pi\kappa\gamma$ . We use a typical value of  $e^2/2\pi\kappa\gamma = 0.15$ , which approximately corresponds to the case of graphene on  $\text{SiO}_2$  substrate [96]. Since this value is also reasonable for carbon nanotubes [91–95], we use it for nanotubes. In numerical calculations,  $V(w, w'; k)$  is obtained by solving simultaneous linear equations given by discretizing position in the direction of the width in Eq. (22).

#### E. Excited states with electron correlations

In the RPA [97,98], the ground state  $|G\rangle$  is assumed to include multiple electrons and holes because of electron correlations. Thus low energy excited states are assumed to be linear combinations of states realized not only by creation of an electron-hole (e-h) pair to the ground state but also by annihilation of an e-h pair to the ground state. Excited states are written as  $|\nu\rangle = Q_\nu^\dagger |G\rangle$ , where creation operators of the excited states  $Q_\nu^\dagger$  are given by [97,98]

$$Q_\nu^\dagger = \sum_{m,i} X_{mi} a_m^\dagger b_i^\dagger - \sum_{m,i} Y_{mi} b_i a_m, \quad (27)$$

with  $a_m$  ( $b_i$ ) and  $a_m^\dagger$  ( $b_i^\dagger$ ) being annihilation and creation operators, respectively, of an electron state  $m$  (a hole one  $i$ ) and  $X_{mi}$  and  $Y_{mi}$  being expansion coefficients. It should be noted that this  $\nu$  is different from that in Eq. (15). The expansion coefficients are determined by an RPA equation [97,98], where excitation energies  $\hbar\Omega_\nu$  for states  $\nu$  with  $\hbar = h/2\pi$  and  $h$  being the Planck constant are also given. In the RPA equation, matrix elements of the Coulomb interactions consist of two terms as

$$\bar{v}_{(r;t)(s;u)} = g_s v_{(r;t)(s;u)}^{(1)} + v_{(r;t)(s;u)}^{(2)}, \quad (28)$$

with  $t$  and  $u$  being initial one-particle states,  $r$  and  $s$  being final ones, and

$$v_{(r;t)(s;u)}^{(1)} = v_{0,(r;t)(s;u)}, \quad v_{(r;t)(s;u)}^{(2)} = -v_{(r;u)(s;t)}. \quad (29)$$

The interactions  $v_{(r;t)(s;u)}^{(1)}$  consist of the bare Coulomb interactions and describe depolarization effects including plasmons [99–101]. On the other hand,  $v_{(r;t)(s;u)}^{(2)}$  is given by the screened Coulomb interactions as shown by Sham and Rice [102] and

shown in various systems [103–110], where the negative sign appears because of exchange of the initial states  $t$  and  $u$  as compared to those of  $v_{(r;t)(s;u)}^{(1)}$ , leading to binding of electrons and holes of excitons. The RPA can reasonably describe excited states in graphene [111] and carbon nanotubes [59,112]. It should be noted that the RPA in the present study is different from that usually used in solid state physics in a sense that the former includes effects of  $v_{(r;t)(s;u)}^{(2)}$  while the latter does not.

### F. Optical absorption

Diagonal components of the dynamical conductivity for a wave vector  $k$  in the direction of nanoribbons are given from the Kubo formula by [113]

$$\begin{aligned} \sigma_{\mu\mu}(w, w'; k) &= -\frac{ie^2 g_s}{\hbar A} \sum_v \delta_{k_v, k} \frac{1}{\Omega_v} \left[ \frac{\langle G | \hat{v}_\mu(w; k) | v \rangle \langle v | \hat{v}_\mu(w'; k) | G \rangle}{\Omega_v - \tilde{\omega} - i\Gamma/\hbar} \right. \\ &\quad \left. - \frac{\langle G | \hat{v}_\mu(w'; k) | v \rangle \langle v | \hat{v}_\mu(w; k) | G \rangle}{\Omega_v + \tilde{\omega} + i\Gamma/\hbar} \right], \end{aligned} \quad (30)$$

where  $\mu = \{x, y\}$ ,  $\hat{v}_\mu(w; k)$  is the  $\mu$  component of the velocity operator for a position  $w$  and  $k$ ,  $k_v$  is a wave vector of an excited state  $|v\rangle$ , and  $\Gamma$  is phenomenological energy broadening. When excited states calculated in the RPA, which include depolarization effects, are used in Eq. (30), the dynamical conductivity describes the response not to self-consistent electric fields, which electrons actually feel, but to external electric fields. We denote this conductivity as  $\tilde{\sigma}_{\mu\mu}(w, w'; k)$ . When excited states calculated in the RPA where  $v_{(r;t)(s;u)}^{(1)}$  is eliminated are used in Eq. (30), the dynamical conductivity gives that without depolarization effects, which describes the response to self-consistent electric fields. We denote this conductivity as  $\sigma_{\mu\mu}(w, w'; k)$ .

When an external electric field with a wave vector  $k$  along nanoribbons is applied to the nanoribbons, optical absorption power is given by [114,115]

$$P = \frac{1}{2W} \text{Re} \left[ \sum_\mu \int_0^W dw j_\mu(w; k) E_\mu^*(w; k) \right], \quad (31)$$

where  $j_\mu(w; k)$  and  $E_\mu(w; k)$  are the  $\mu$  components of a current density and a self-consistent electric field, respectively, for  $w$  and  $k$ . Thus the self-consistent electric field is necessary for calculations of the optical absorption power. A method to calculate Eq. (31) is as follows: The current density is given by the product of the conductivity without depolarization effects  $\sigma_{\mu\mu}(w, w'; k)$  and the self-consistent electric field  $E_\mu(w; k)$  or that of the conductivity with depolarization effects  $\tilde{\sigma}_{\mu\mu}(w, w'; k)$  and the external electric field  $E_{0,\mu}(w; k)$ . That is, the following relation exists:

$$\begin{aligned} j_\mu(w; k) &= \int_0^W dw' \sigma_{\mu\mu}(w, w'; k) E_\mu(w'; k) \\ &= \int_0^W dw' \tilde{\sigma}_{\mu\mu}(w, w'; k) E_{0,\mu}(w'; k), \end{aligned} \quad (32)$$

where we assume that the conductivity tensors are diagonal and the external electric field is along the  $\mu$  direction. Therefore, from the second equality of (32), the

self-consistent electric field is obtained by using  $\sigma_{\mu\mu}(w, w'; k)$  and  $\tilde{\sigma}_{\mu\mu}(w, w'; k)$ . As a result, for a constant external electric field  $E_{0,\mu}(w; k) = E_0$ , we have

$$P = \frac{|E_0|^2}{2} \text{Re} \tilde{\sigma}_{\mu\mu}, \quad (33)$$

with

$$\begin{aligned} \tilde{\sigma}_{\mu\mu} &= \frac{1}{W} \int_0^W dw \left[ \int_0^W dw' \tilde{\sigma}_{\mu\mu}(w, w'; k) \right] \\ &\quad \times \left[ \int_0^W dw' \int_0^W dw'' \sigma_{\mu\mu}^{-1*}(w, w'; k) \tilde{\sigma}_{\mu\mu}^*(w', w''; k) \right], \end{aligned} \quad (34)$$

where  $\sigma_{\mu\mu}^{-1}(w, w'; k)$  is the inverse function of  $\sigma_{\mu\mu}(w, w'; k)$ , which is numerically calculated on the basis of discretized positions or plane waves. The optical absorption is characterized by the real part of  $\tilde{\sigma}_{\mu\mu}$ . On the other hand, since  $\tilde{\sigma}_{\mu\mu}(w, w'; k)$  includes depolarization effects, we expect that  $\tilde{\sigma}_{\mu\mu}(w, w'; k)$  itself characterizes optical absorption with depolarization effects. Thus we define an averaged conductivity as

$$\langle \tilde{\sigma}_{\mu\mu} \rangle = \frac{1}{W} \int_0^W dw \int_0^W dw' \tilde{\sigma}_{\mu\mu}(w, w'; k). \quad (35)$$

Difference between  $\tilde{\sigma}_{\mu\mu}$  and  $\langle \tilde{\sigma}_{\mu\mu} \rangle$  is discussed in Sec. IV.

The conductivities  $\tilde{\sigma}_{\mu\mu}$  and  $\langle \tilde{\sigma}_{\mu\mu} \rangle$  are functions of  $k$  and  $\tilde{\omega}$ . Since the wave vectors of electromagnetic waves are usually much smaller than those of electrons, optical absorption spectra are given by  $\tilde{\sigma}_{\mu\mu}$  with  $k \approx 0$ . To measure  $\tilde{\sigma}_{\mu\mu}$  with finite  $k$ , light with finite  $k$ , which can be caused by near fields, for example, is needed [116]. Although phenomenological energy broadening in Eq. (30) depends on situations, we use values of the order of  $0.01 \times (2\pi\gamma/W)$  as typical ones, which are several millielectron volts for widths of several nanometers and typical for carbon nanotubes [117–121].

### G. Selection rule

A selection rule for optical transitions is not simple in graphene nanoribbons with electron correlations and depolarization effects because of mixing of states in different energy bands and the complex expression of the conductivity in Eq. (34). To understand numerical results in the next section, we review a selection rule for nanoribbons without electron correlations and depolarization effects, which is still useful and has been reported in many studies [31,33,35,36]. In this case, optical absorption spectra are characterized by  $\langle \tilde{\sigma}_{\mu\mu} \rangle$  in Eq. (35), where the velocity matrix elements in Eq. (30), which determine a selection rule, are replaced by those between electron states and hole ones in the one-particle model. Derivation of the following selection rule based on the effective-mass approximation is given in Appendix A.

For armchair nanoribbons, we consider optical transitions between band edges at  $k_y = 0$ , which play an important role because of the divergence of the density of states. A selection rule for parallel polarization, where the direction of light polarization is along nanoribbons, is as follows: In semiconducting nanoribbons, transitions from a valence band  $vi$  to a conduction band  $ci$  with the same  $i$  are allowed. The other

transitions between the valence and conduction bands and all transitions between valence bands and between conduction bands are prohibited. In metallic nanoribbons, only transitions between valence and conduction bands with  $vi$  and  $ci$ , respectively, except for the linear dispersions are allowed.

For perpendicular polarization, where the direction of light polarization is perpendicular to nanoribbons, a selection rule is as follows: In semiconducting nanoribbons, transitions are allowed between valence and conduction bands  $vi$  and  $cj$ , respectively, with even  $i$  and odd  $j$  and with odd  $i$  and even  $j$  while intravalence (intraconduction) band transitions are allowed between  $vi$  and  $vj$  ( $ci$  and  $cj$ ) with even  $i$  and even  $j$  and with odd  $i$  and odd  $j$ , except for the case of  $k_x - k'_x = 2n\pi/W$ , where  $k_x$  and  $k'_x$  are wave vector components along the width for initial and final states, respectively, and  $n$  denotes integers. In metallic nanoribbons, except for the linear dispersions, transitions between any energy bands are allowed although final states are limited to either of doubly degenerate states. For the linear dispersions, transitions from the Dirac point to the other energy bands with  $k'_x \neq 2n\pi/W$  can be allowed by taking either of the limits of  $k_y \rightarrow \pm 0$ .

For zigzag nanoribbons, we have the following selecting rule: For parallel polarization, transitions between the valence and conduction bands with  $vi$  and  $cj$ , respectively, are allowed for odd  $i$  and even  $j$  and for even  $i$  and odd  $j$  while intravalence (intraconduction) band transitions between  $vi$  and  $vj$  ( $ci$  and  $cj$ ) are allowed for odd  $i$  and odd  $j$  and for even  $i$  and even  $j$ . For perpendicular polarization, a selection rule is that for parallel polarization where the rule for indices  $i$  and  $j$  for transitions between the valence and conduction bands is exchanged with that for intravalence band transitions and intraconduction band ones.

### III. NUMERICAL RESULTS

#### A. Screening of the Coulomb interactions

In numerical calculations in Secs. III and IV, we choose semiconducting armchair nanoribbons with  $N = 46$  ( $\delta = 1$ ), metallic armchair ones with  $N = 47$  ( $\delta = 0$ ), and zigzag ones with  $N = 27$  as typical nanoribbons, where excitons and plasmons manifest themselves mainly in infrared frequencies. These three nanoribbons have similar widths as  $W = 5.5$  nm and  $5.7$  nm for the armchair nanoribbons with  $N = 46$  and  $47$ , respectively, and  $W = 5.6$  nm for the zigzag nanoribbons. For metallic armchair and zigzag nanoribbons, energy gaps open at the Fermi energy by effects originating from edges [5,6], which are not included in the preset model. However, the energy gaps are small for the above nanoribbons, about 40 meV for the  $N = 47$  armchair nanoribbons [6], for example, and are considered to be safely neglected in doped cases. Thus we only study those cases for the metallic armchair and zigzag nanoribbons. Since the energy bands of nanoribbons are symmetric with respect to the origin of energy, electron doping is only considered.

Figure 3 shows the static electric susceptibility normalized by the Coulomb interaction parameter  $\chi(w, w'; k)(e^2/2\pi\kappa\gamma)^{-1}$  as a function of  $w'$  for various values of  $w$  and  $k$ . Results of the semiconducting ( $N = 46$ ) and metallic ( $N = 47$ ) armchair nanoribbons are shown

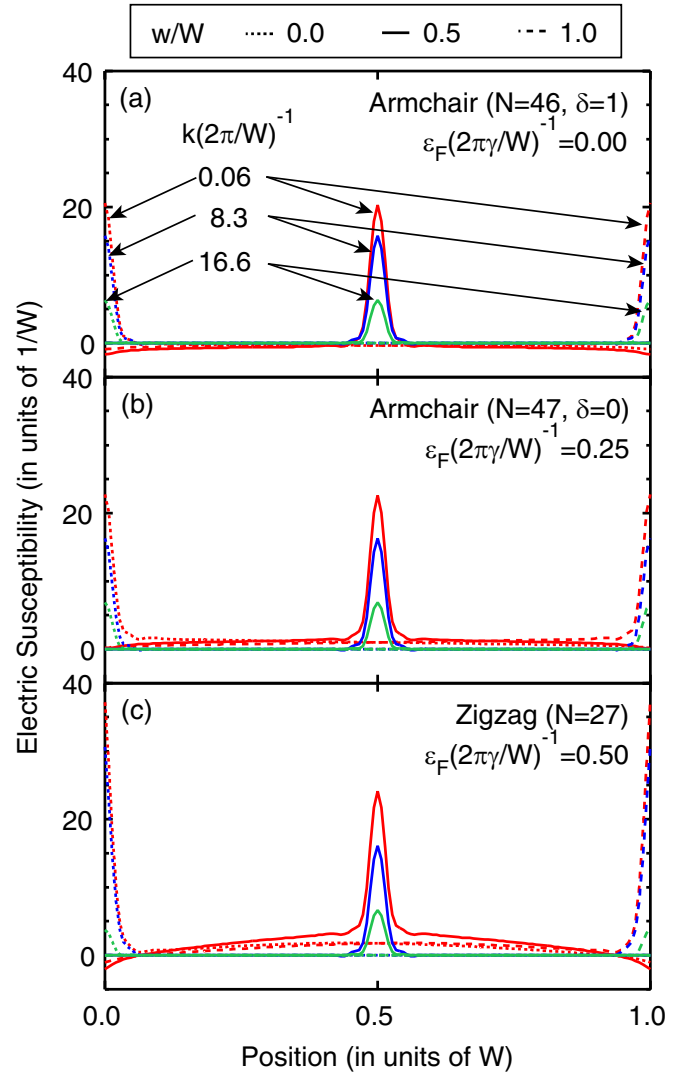


FIG. 3. Static electric susceptibility  $\chi(w, w'; k)$  normalized by  $e^2/2\pi\kappa\gamma$  as a function of  $w'$  for various  $w$  and  $k$  for (a) the semiconducting armchair nanoribbon with  $N = 46$ , (b) the doped metallic armchair nanoribbon with  $N = 47$ , and (c) the doped zigzag nanoribbon with  $N = 27$ . In (a), (b), and (c), results for  $k(2\pi/W)^{-1} = 0.06, 8.3,$  and  $16.6$  are shown as indicated by arrows in (a). The Fermi energy is  $\varepsilon_F(2\pi\gamma/W)^{-1} = 0$  in (a),  $0.25$  in (b), and  $0.5$  in (c). Solid lines denote results for  $w/W = 0.5$  and dotted and dashed lines are those for  $w/W = 0$  and  $1$ , respectively.

in Figs. 3(a) and 3(b), respectively, and that of the zigzag nanoribbon with  $N = 27$  is shown in Fig. 3(c). The Fermi energy is chosen as  $\varepsilon_F(2\pi\gamma/W)^{-1} = 0$  in Fig. 3(a) and  $\varepsilon_F(2\pi\gamma/W)^{-1} = 0.25$  and  $0.5$  in Figs. 3(b) and 3(c), respectively, where in Figs. 3(b) and 3(c), the Fermi energy only crosses the lowest conduction band. In Fig. 3(a) for the semiconducting armchair nanoribbon, when  $w$  is located at the center of the nanoribbon ( $w/W = 0.5$ ), the susceptibility denoted by solid lines takes maximum values at  $w' = w$  and rapidly decreases as  $w'$  deviates from  $w$ , where the peak value decreases with the increase of  $k$ . For small  $k$  [ $k(2\pi/W)^{-1} = 0.06$ ], the susceptibility is negative for  $w'$  away from  $w$ , suggesting that the Coulomb potential can be

enhanced by surrounding electrons, i.e., antiscreened. This behavior is rapidly suppressed as  $k$  increases.

The result of the susceptibility can be explained by Eq. (25). Since  $\mathbf{F}_r(w)$  and  $\mathbf{F}_t(w)$  are linear combinations of plane waves, the right-hand side of Eq. (25) is a form similar to the Fourier transform, where the integral part indicates coefficients for plane waves given by  $\mathbf{F}_r^\dagger(w')\mathbf{F}_r(w')$ , whose wave vectors are differences and sums of those in the width direction for states  $r$  and  $t$  and small for small differences between the energy band indices for  $r$  and  $t$ . For  $k \ll 1/W$ , since  $K_0(z) \approx -\log(z/2)$  for  $z \ll 1$ , various  $w''$  in  $0 \leq w'' \leq W$  can contribute to the integral. However, since  $\mathbf{F}_r^\dagger(w'')\mathbf{F}_r(w'')$  is an oscillating function, in the relatively long-range region of  $|w - w'| \sim W$ ,  $\mathbf{F}_r^\dagger(w'')\mathbf{F}_r(w'')$  with wave vectors larger than  $\sim 1/W$  cancel out and those with small wave vectors of the order of  $1/W$  only give finite values, leading to gradually oscillating components as a function of  $w - w'$  with negative values. On the other hand, for  $k \gg 1/W$ , since  $K_0(z) \approx \sqrt{\pi/2z}e^{-z}$  for  $z \gg 1$ ,  $w''$  close to  $w$  only contributes to the integral, where various  $\mathbf{F}_r^\dagger(w'')\mathbf{F}_r(w'')$  with wave vectors in a wide range exist in the integral. Thus the value of the susceptibility is localized around  $w' \sim w$  and reduced with the increase of  $k$  because of exponentially small  $K_0(z)$ . Results for  $w$  located at edges with  $w/W = 0$  and  $1$ , which are denoted by dotted and dashed lines, respectively, are similar to the case of  $w/W = 0.5$ .

In Fig. 3(b) for the metallic armchair nanoribbon, results are similar to those of Fig. 3(a) except that negative values do not appear. This is because for free electrons in the conduction band, intraband transitions between states  $r$  and  $t$  in Eq. (25) largely contribute to the susceptibility as the Fourier components with zero wave vector, i.e., constants, leading to upward shift of the susceptibility and the disappearance of negative values. In Fig. 3(c) for the zigzag nanoribbon, results are similar to those in Fig. 3(b). In this case, the susceptibility for small  $k$  [ $k(2\pi/W)^{-1} = 0.06$ ] takes negative values for  $w'$  near edges. This is probably because of edge states.

Figure 4 shows the screened Coulomb potential  $V(w, w'; k)$  for (a) the  $N = 46$  semiconducting armchair nanoribbon and (b) the  $N = 27$  zigzag nanoribbon as a function of  $w'$  for various  $w$  and  $k$ . The bare Coulomb potential  $V_0(w, w'; k)$  is also plotted in the figure, where the divergence of the potential is properly suppressed because of discretization of position [7]. In Fig. 4(a) corresponding to the case of Fig. 3(a), the potential for a small wave vector [ $k(2\pi/W)^{-1} = 0.06$ ] and  $w$  located at the center ( $w/W = 0.5$ ), which is denoted by a solid line, is reduced near  $w' = w$  as compared to the bare Coulomb potential but changes to be increased for  $w'$  away from  $w$ , i.e., antiscreened, as suggested in Fig. 3(a). When the wave vector increases [ $k(2\pi/W)^{-1} = 8.3$ ], the potential rapidly decreases and the antiscreening effect vanishes. Results for  $w$  located at edges ( $w/W = 0$  and  $1$ ) are similar. Antiscreening effects were reported for low dimensional systems [90, 122–124]. For the doped zigzag nanoribbon in Fig. 4(b), which corresponds to the case of Fig. 3(c), the potential for  $k(2\pi/W)^{-1} = 0.06$  is strongly suppressed as compared to that in Fig. 4(a) because of strong screening arising from free electrons. Similar results are obtained for doped semiconducting and metallic armchair nanoribbons (not shown). A screening effect characteristic

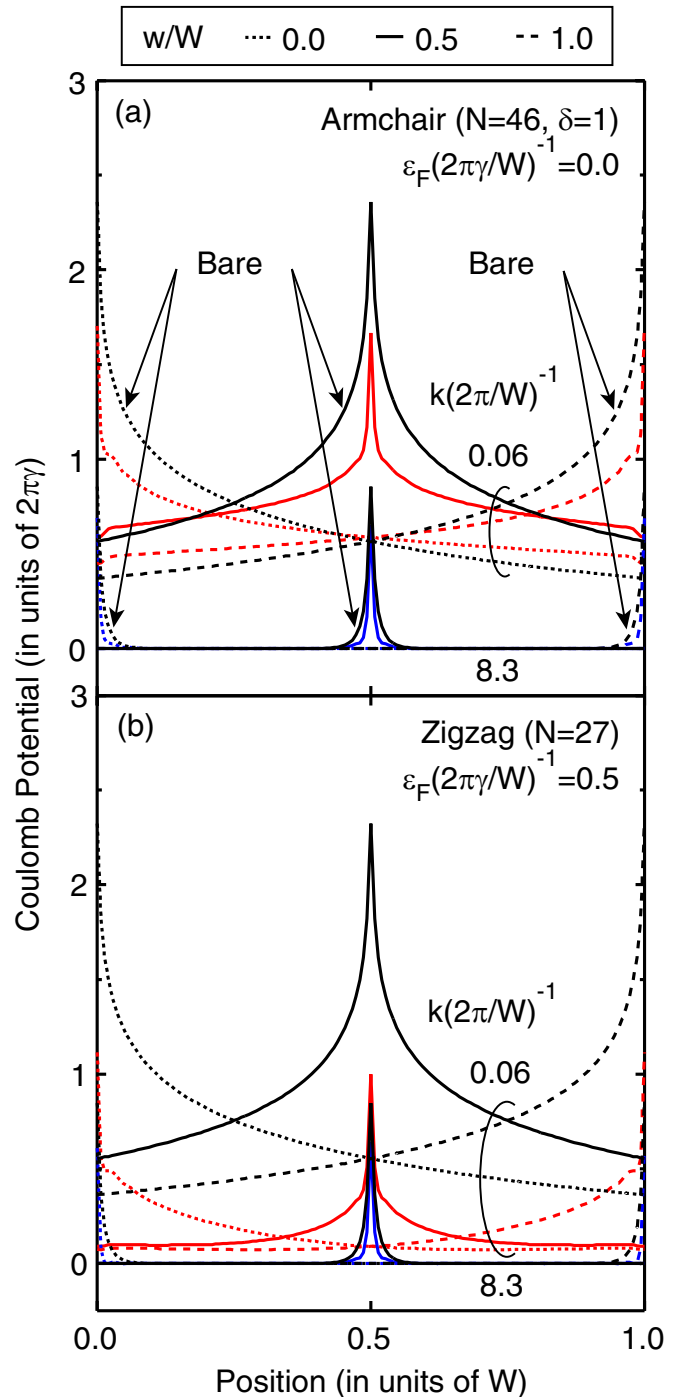


FIG. 4. Screened Coulomb potential  $V(w, w'; k)$  as a function of  $w'$  for various  $w$  and  $k$  for (a) the semiconducting armchair nanoribbon with  $N = 46$  and (b) the doped zigzag nanoribbon with  $N = 27$ . Solid, dotted, and dashed lines are used in a similar manner to those in Fig. 3. Results for  $k(2\pi/W)^{-1} = 0.06$  and  $8.3$  are shown and  $\varepsilon_F(2\pi\gamma/W)^{-1} = 0$  in (a) and  $0.5$  in (b). In (a) and (b), the bare Coulomb potential  $V_0(w, w'; k)$  is also plotted as indicated by arrows in (a), for comparison.

to zigzag nanoribbons is that the Coulomb potential for  $w$  located at edges is relatively strongly suppressed for  $w' \approx w$  as compared to that for armchair nanoribbons because of edge states.

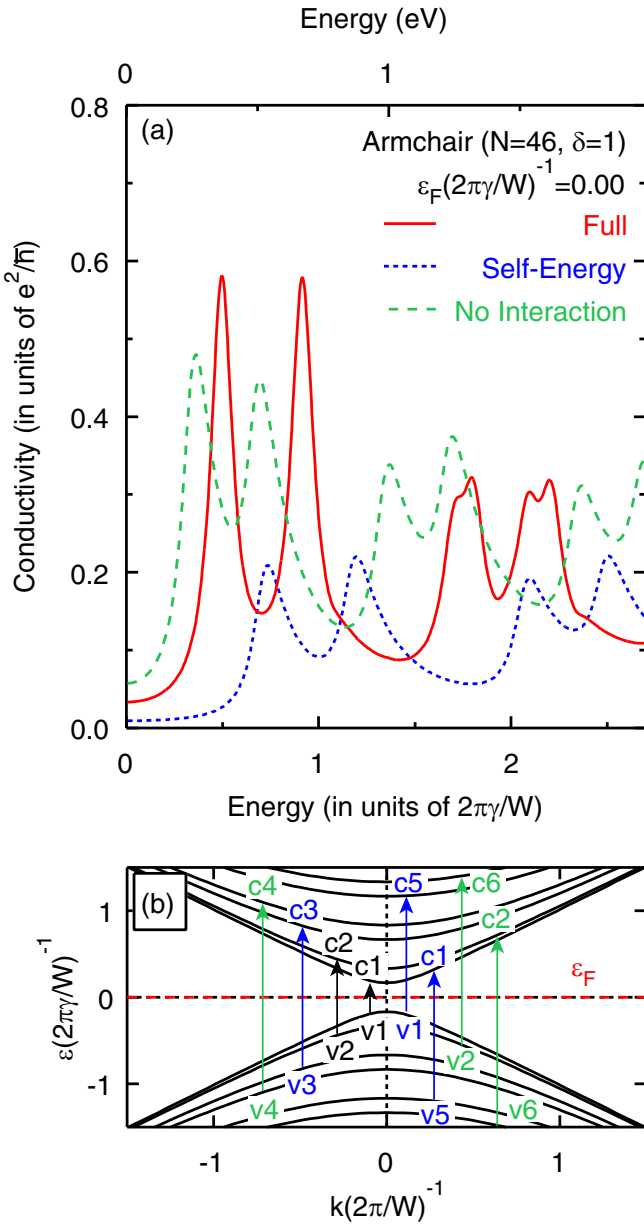


FIG. 5. (a) Energy dependence of the real part of the conductivity  $\text{Re}\tilde{\sigma}_{yy}$  with  $k = 0$  for the semiconducting armchair nanoribbon with  $N = 46$ , where  $\Gamma(2\pi\gamma/W)^{-1} = 0.07$ . A solid line shows a result with full interactions and dotted and dashed lines are those with only self-energy and no interactions, respectively. An upper horizontal axis is in units of eV for  $\gamma = \sqrt{3}a\gamma_0/2$  with  $\gamma_0 = 3.03$  eV being a resonance integral for nearest-neighboring  $\pi$  orbitals [96]. (b) Schematic illustration of energy bands of the armchair nanoribbon in (a). A horizontal dashed line indicates the Fermi energy. Arrows denote optical transitions associated with peaks in (a).

### B. Optical absorption of armchair nanoribbons

Figure 5(a) shows the real part of the conductivity  $\text{Re}\tilde{\sigma}_{yy}$  with  $k = 0$  for the nondoped semiconducting armchair nanoribbon with  $N = 46$  for parallel polarization. A solid line is a result with full interactions in the RPA, a dotted line is that only including self-energy as electron-electron interactions, and a dashed line is that with no interactions. Comparing

energy band gaps without and with interactions, which are approximately given by energies of the lowest peaks for the dashed and dotted lines, respectively, the self-energy considerably enhances the band gap by a factor of about two. This seems to be consistent with band gap enhancement with large self-energy corrections in first-principles calculations [125].

For the solid line, the lowest two peaks in energy arise from excitons mainly associated with transitions from  $v_1$  to  $c_1$  and from  $v_2$  to  $c_2$ , which are schematically shown in Fig. 5(b). The third lowest peak mainly comes from an exciton for transitions between  $v_3$  and  $c_3$  [see Fig. 5(b)]. This peak splits because of the following: Transition energy between the band edges of the energy bands  $v_3$  and  $c_3$  is the same as those between  $v_5$  and  $c_1$  and between  $v_1$  and  $c_5$  [see Fig. 5(b)]. Thus, the exciton for the transitions between  $v_3$  and  $c_3$  can interact with an exciton associated with the transitions between  $v_1$  and  $c_5$  and between  $v_5$  and  $c_1$ , leading to the splitting of the peak. It should be noted that optical transition to the latter exciton is prohibited, i.e., the latter exciton is dark. Similar splitting occurs for the fourth lowest peak, where an exciton for transitions from  $v_4$  to  $c_4$  interacts with a dark exciton for transitions from  $v_2$  to  $c_6$  and from  $v_6$  to  $c_2$  [see Fig. 5(b)]. The splitting of the peaks cannot be explained within one-particle pictures as shown in the results with the dotted and dashed lines and is never seen in carbon nanotubes. Since the splitting is associated with the high and low energy bands, its observation may need nanoribbons with widths larger than several nanometers, where the effective-mass approximation is valid around the tops or bottoms of the energy bands  $v_5$ ,  $v_6$ ,  $c_5$ , and  $c_6$ .

Effects of carrier doping are shown for the same armchair nanoribbon in Fig. 6. Figures 6(a) and 6(b) show  $\text{Re}\tilde{\sigma}_{yy}$  with zero and finite  $k$  for parallel polarization. The Fermi energy is  $\varepsilon_F(2\pi\gamma/W)^{-1} = 0.25$  and  $0.5$  in Figs. 6(a) and 6(b), respectively, which crosses the lowest and the lowest two conduction bands for the former and the latter, respectively [see Figs. 6(d) and 6(e)]. In Fig. 6(a), for a small finite wave vector  $k(2\pi/W)^{-1} = 0.11$ , a large peak arising from a plasmon appears at an energy of  $\hbar\tilde{\omega}(2\pi\gamma/W)^{-1} \approx 0.17$ , which is associated with intraband transitions in the conduction band  $c_1$  and decreases as  $k$  increases. The exciton peak for the transitions from  $v_1$  to  $c_1$  disappears near  $k = 0$  because of the reduced number of the associated transitions by doping while the other exciton peaks remain. The splitting of the second lowest peak [the third lowest peak in Fig. 5(a)] for  $k = 0$  is smeared because of reduction of the transitions from  $v_5$  to  $c_1$ , where the transitions from  $v_1$  to  $c_5$  still remain, leading to slight broadening of the peak. In Fig. 6(b), peaks arising from the plasmons for small  $k$  are more prominent than those in Fig. 6(a) because the electron density at the Fermi energy increases. The disappearance of the splitting of the second lowest exciton peak [the fourth lowest peak in Fig. 5(a)] arises for a similar reason to the reason for that of the second lowest peak in Fig. 6(a).

Figure 6(c) shows the Fermi-energy dependence of  $\text{Re}\tilde{\sigma}_{xx}$  with  $k = 0$  for perpendicular polarization. For no doping with  $\varepsilon_F = 0$ , a solid line for  $\Gamma(2\pi\gamma/W)^{-1} = 0.07$  shows a small peak at  $\hbar\tilde{\omega}(2\pi\gamma/W)^{-1} \approx 0.76$ , which is due to an exciton associated with transitions from  $v_1$  to  $c_2$  and from  $v_2$  to  $c_1$ . To show the exciton more clearly, a result for smaller energy

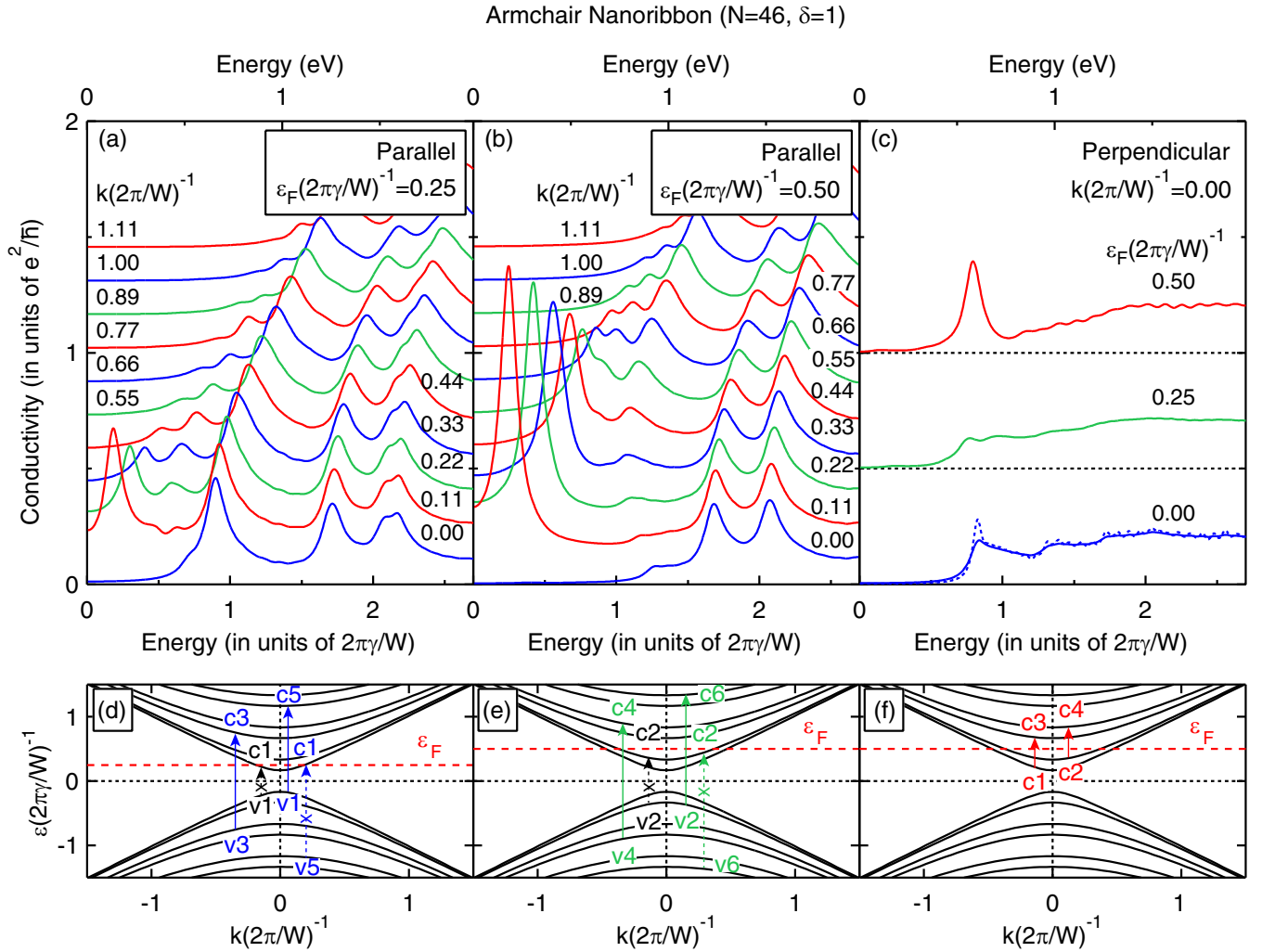


FIG. 6. (a) and (b) Energy dependence of  $\text{Re}\delta_{yy}$  for the doped semiconducting armchair nanoribbons with  $N = 46$  for parallel polarization, where  $\varepsilon_F(2\pi\gamma/W)^{-1} = 0.25$  in (a) and 0.5 in (b). Results for various  $k$  are plotted by shifting the origin of the vertical axes for clarity. (c) Energy dependence of  $\text{Re}\delta_{xx}$  for the semiconducting armchair nanoribbons with  $N = 46$  for perpendicular polarization in the case of  $k = 0$ . Results for  $\varepsilon_F(2\pi\gamma/W)^{-1} = 0, 0.25$ , and 0.5 are shown by shifting the origin of the vertical axis for clarity. In (a)–(c),  $\Gamma(2\pi\gamma/W)^{-1} = 0.07$  for solid lines and 0.04 for a dotted line in (c) and upper horizontal axes are plotted in the same way as that in Fig. 5(a). (d)–(f) Schematic illustrations of optical transitions associated with peaks in (a)–(c), where (d) corresponds to (a), (e) to (b), and (f) to (c). Horizontal dashed lines indicate the Fermi energy, arrows with solid lines denote allowed transitions, and those with dashed lines and crosses describe prohibited transitions.

broadening of  $\Gamma(2\pi\gamma/W)^{-1} = 0.04$  is also shown by a dotted line. Although the joint density of states for these transitions gives a large peak, depolarization effects considerably suppress optical absorption for these transitions. However, strong exciton effects cause the peak structure. This mechanism is the same as cross-polarized excitons in carbon nanotubes [9,11,99,126,127]. For the doped case of  $\varepsilon_F(2\pi\gamma/W)^{-1} = 0.25$ , the exciton peak vanishes because energy for the transitions associated with the exciton is in a one-particle excitation continuum for transitions between  $c1$  and  $c3$ .

For further doping of  $\varepsilon_F(2\pi\gamma/W)^{-1} = 0.5$ , a prominent peak appears, which is caused by a plasmon associated with interband transitions between  $c1$  and  $c3$  and between  $c2$  and  $c4$  [see Fig. 6(f)], meaning that the plasmon is polarized in the width direction. On the other hand, plasmons do not appear for  $\varepsilon_F(2\pi\gamma/W)^{-1} = 0.25$  in spite of that transitions from

$c1$  to higher conduction bands are possible. This is due to the following: Plasmons consist of e-h pairs associated with continuum states below the plasmons in energy. For formation of plasmons,  $v_{(r;t)(s;u)}^{(1)}$  in Eq. (29) is essential, which includes factors like  $\mathbf{F}_r^\dagger(w)\mathbf{F}_t(w)$  in Eq. (26). For an e-h pair with an electron state  $m$  and a hole one  $i$ , the factor appears as  $\mathbf{F}_m^\dagger(w)\mathbf{F}_i(w)$  or its complex conjugate. This is negligible for  $k(2\pi/W)^{-1} \ll 1$  because of a nature of Dirac electrons when the parity of the band index for the electron is different from that for the hole for intravalence band and intraconduction band transitions as can be seen from Eqs. (4), (10), and (12). For  $\varepsilon_F(2\pi\gamma/W)^{-1} = 0.25$ , the factors are non-negligible for transitions from  $c1$  to  $c3, c5, \dots$ . However, there is no energy gap above one-particle excitation continuums for the transitions, whose upper boundaries are in continuum states for transitions between the valence and conduction bands. For

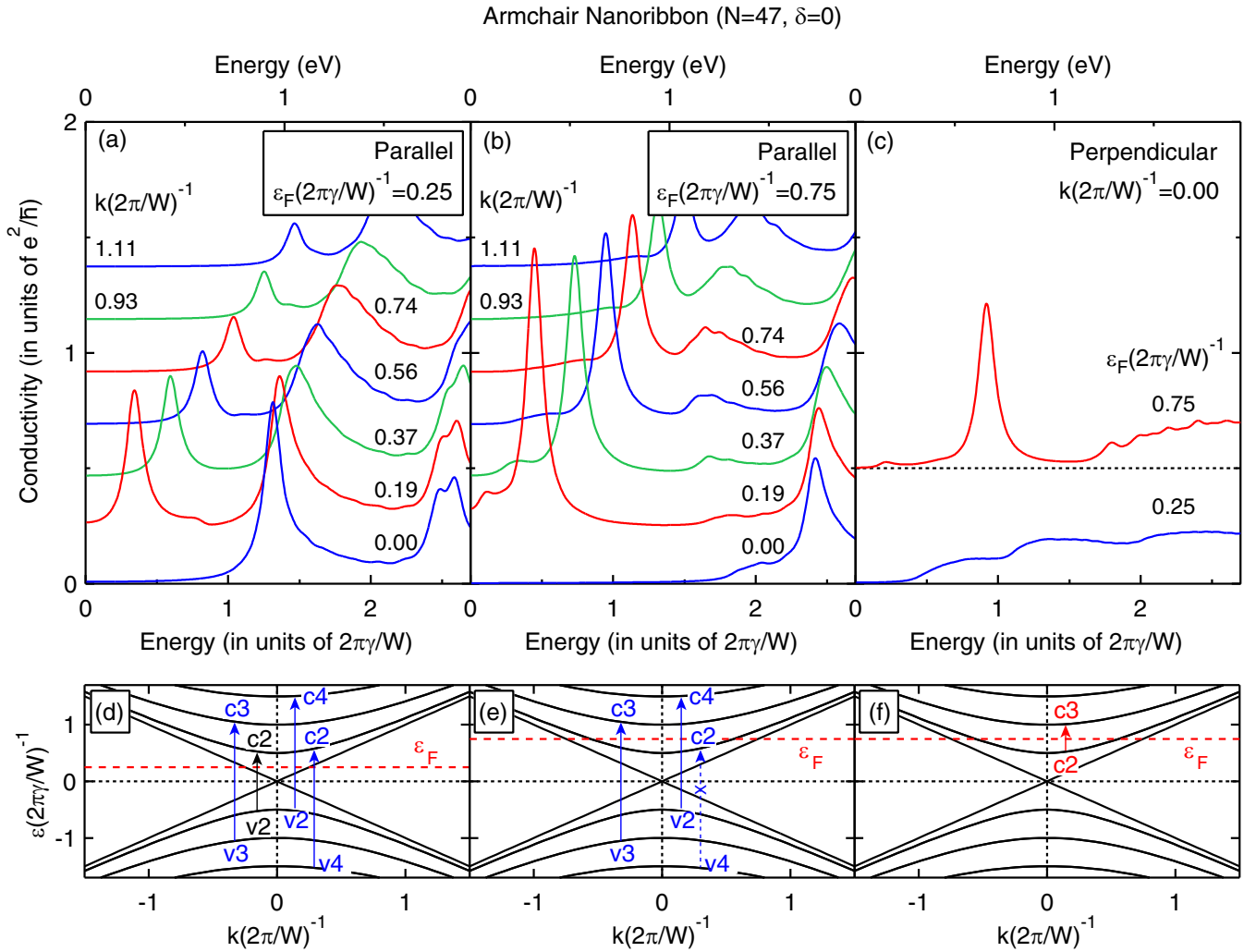


FIG. 7. (a) and (b) Energy dependence of  $\text{Re}\delta_{yy}$  for the doped metallic armchair nanoribbons with  $N = 47$  for parallel polarization, where  $\epsilon_F(2\pi\gamma/W)^{-1} = 0.25$  in (a) and  $0.75$  in (b). (c) Energy dependence of  $\text{Re}\delta_{xx}$  for the doped metallic armchair nanoribbons with  $N = 47$  for perpendicular polarization in the case of  $k = 0$ . Results for  $\epsilon_F(2\pi\gamma/W)^{-1} = 0.25$  and  $0.75$  are shown. In (a)–(c),  $\Gamma(2\pi\gamma/W)^{-1} = 0.07$ . (d)–(f) Schematic illustrations of optical transitions. All the panels are plotted in a similar way to those in Fig. 6.

$\epsilon_F(2\pi\gamma/W)^{-1} = 0.5$ , an energy gap opens above the one-particle excitation continuum for the transitions from  $c1$  to  $c3$  and from  $c2$  to  $c4$ , leading to the plasmon. The situation is similar to plasmons for perpendicular polarization in doped semiconducting carbon nanotubes [59–62].

Figure 7 is a similar plot for the metallic armchair nanoribbon with  $N = 47$  to Fig. 6. The Fermi energy crosses the conduction band  $c1$  for  $\epsilon_F(2\pi\gamma/W)^{-1} = 0.25$  and  $c1$  and  $c2$  for  $\epsilon_F(2\pi\gamma/W)^{-1} = 0.75$  [see Figs. 7(d) and 7(e)]. Results in Figs. 7(a) and 7(b) are similar to those in Figs. 6(a) and 6(b), respectively. For parallel polarization in Fig. 7(a), the lowest and the second lowest peaks for  $k = 0$  arise from excitons associated with transitions from  $v2$  to  $c2$  and from  $v3$  to  $c3$ , respectively, where the latter peak splits because of interaction with a dark exciton associated with transitions from  $v2$  to  $c4$  and from  $v4$  to  $c2$  [see Fig. 7(d)]. The splitting disappears in Fig. 7(b) because of suppression of the transitions from  $v4$  to  $c2$  [see Fig. 7(e)]. The manifestation of the excitons in metallic nanoribbons is similar to that in metallic carbon nanotubes [7, 128–130]. Peaks arising from plasmons in Fig. 7(a)

for finite  $k$  are enhanced with the increase of the Fermi energy as shown in Fig. 7(b).

For perpendicular polarization in Fig. 7(c), there is no peak for  $\epsilon_F(2\pi\gamma/W)^{-1} = 0.25$  while a prominent plasmon peak appears for  $\epsilon_F(2\pi\gamma/W)^{-1} = 0.75$ . The nonexistence of plasmons for  $\epsilon_F(2\pi\gamma/W)^{-1} = 0.25$  is because there is no energy gap above the upper boundary of the one-particle excitation continuum for transitions from  $c1$  to  $c2$ , which is continuously connected to continuum states for transitions from  $v1$  to  $c2$ . For  $\epsilon_F(2\pi\gamma/W)^{-1} = 0.75$ , an energy gap appears above a one-particle excitation continuum for transitions from  $c2$  to  $c3$  [see Fig. 7(f)]. For these transitions,  $v_{(r,t)(s,u)}^{(1)}$  is finite, leading to the plasmon. The situation is similar to plasmons for perpendicular polarization in doped metallic carbon nanotubes [59–62].

### C. Optical absorption of zigzag nanoribbons

Figure 8 shows calculated results for the doped zigzag nanoribbons with  $N = 27$ , which is presented in a similar way

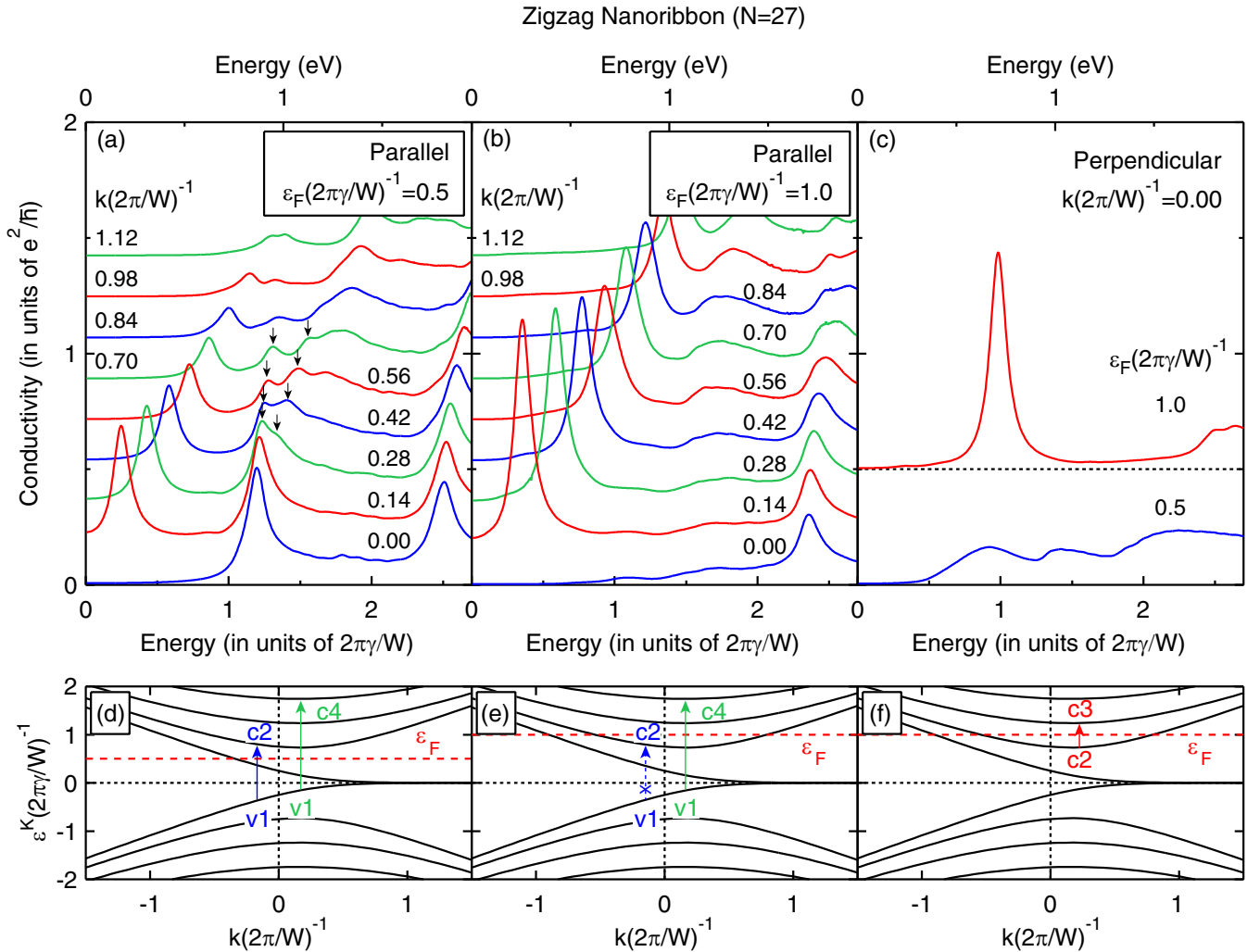


FIG. 8. (a) and (b) Energy dependence of  $\text{Re}\bar{\sigma}_{xx}$  for the doped zigzag nanoribbons with  $N = 27$  for parallel polarization, where  $\varepsilon_F(2\pi\gamma/W)^{-1} = 0.5$  in (a) and 1.0 in (b). In (a), arrows indicate splitting of a peak associated with edge states. (c) Energy dependence of  $\text{Re}\bar{\sigma}_{yy}$  for the doped zigzag nanoribbons with  $N = 27$  for perpendicular polarization in the case of  $k = 0$ . Results for  $\varepsilon_F(2\pi\gamma/W)^{-1} = 0.5$  and 1.0 are shown. In (a)–(c),  $\Gamma(2\pi\gamma/W)^{-1} = 0.07$ . (d)–(f) Schematic illustrations of optical transitions at the  $K$  point. All the panels are plotted in a similar way to those in Fig. 6.

to Fig. 6. For parallel polarization in Figs. 8(a) and 8(b) with  $\varepsilon_F(2\pi\gamma/W)^{-1} = 0.5$  and 1.0, respectively, the Fermi energy crosses the conduction band  $c1$  for the former and  $c1$  and  $c2$  for the latter at each valley [see Figs. 8(d) and 8(e)]. The optical absorption spectra in Figs. 8(a) and 8(b) are similar to those in Figs. 7(a) and 7(b), respectively, for the metallic armchair nanoribbons. There are also differences from the results of the metallic armchair nanoribbons. In Fig. 8(a), the first and second lowest exciton peaks at  $k = 0$  arise from transitions between  $v1$  and  $c2$  and those between  $v1$  and  $c4$ , respectively, while in Fig. 7(a), the lowest two peaks at  $k = 0$  come from the transitions between  $v_i$  and  $c_i$  with  $i = \{2, 3\}$ . The lowest exciton peak near  $k = 0$  is almost independent of  $k$  and splits into two peaks with arrows as  $k$  increases. Since the energy bands  $v1$  and  $c1$  are asymmetric about the axis of  $k_x = 0$ , excitation energies for the transitions from  $v1$  to  $c2$  with finite  $k$  at the  $K$  and  $K'$  points separate from each other as  $k$  increases, leading to splitting of the peak. Since the lowest

energy of the transitions associated with the flat parts of the energy bands is almost independent of  $k$ , the lower peak is insensitive to  $k$ . Another different point from Fig. 7(a) is that the second lowest exciton peak at  $k = 0$  in Fig. 8(a) is not split. This is because there are no other transitions for which energy is the same as that for the transitions from  $v1$  to  $c4$  near the band edges of  $c4$ .

Figure 8(c) shows results for perpendicular polarization at  $k = 0$ . For  $\varepsilon_F(2\pi\gamma/W)^{-1} = 0.5$ , no plasmon peak appears because the flat parts of the energy bands  $c1$  lead to no energy gaps opening above one-particle excitation continua for transitions from  $c1$  to higher conduction bands. For  $\varepsilon_F(2\pi\gamma/W)^{-1} = 1.0$ , a prominent plasmon peak occurs because an energy gap opens above a one-particle excitation continuum for transitions from  $c2$  to  $c3$  [see Fig. 8(f)] and because  $v_{(r;t)(s;u)}^{(1)}$  is finite for these transitions. This Fermi-energy dependence of the plasmon is similar to those of the armchair nanoribbons in Figs. 7(c) and 8(c).

#### IV. DISCUSSION

The energy bands of graphene nanoribbons are similar to those of carbon nanotubes as described in Secs. II B and II C. Electronic structure of nanotubes has been mainly revealed by optical methods [7–28,58–62,131–135]. Thus, it is expected that correspondence between the optical properties of nanoribbons and nanotubes gives useful information for study of nanoribbons. In the former part of this section, we compare optical absorption spectra between nanoribbons and nanotubes. To find correspondence between the two materials in a wide range, we describe them in scaling methods. For the results in Sec. III, since all the excitons and the plasmons for perpendicular polarization in the panels (c) of Figs. 6–8 originate from transitions between different energy bands, their energies are approximately scaled by separation between energy bands. On the other hand, this scaling is inapplicable for the plasmons for parallel polarization in the panels (a) and (b) of Figs. 6–8 because they arise from transitions in the same energy bands. Another scaling is necessary for them.

Figure 9 compares optical absorption spectra for the semiconducting nanoribbons and semiconducting nanotubes in Figs. 9(a)–(c) and those for the metallic nanoribbons and metallic nanotubes in Figs. 9(d)–(f). Details of calculations for nanotubes are described in earlier studies [59,112]. Figure 9(a) shows results with no doping and  $k = 0$  for the semiconducting armchair nanoribbon in Fig. 5(a) (solid line) and carbon nanotubes (dashed lines) for parallel polarization, where results for nanotubes with two circumference lengths of  $L \approx W/2$  and  $W$  are shown. A horizontal axis is plotted in units of an energy scale  $\varepsilon_u = \pi\gamma/W$  for the nanoribbon and  $2\pi\gamma/L$  for the nanotubes. In this case, the energy bands of the nanoribbons and nanotubes become the same when the wave vector is properly scaled, as mentioned in Sec. II B. The energies of the two exciton peaks of the nanoribbon approximately agree with those of the nanotubes, where slight deviations come from electron–electron interactions. Since energy broadening is the same in units of usual kinetic energies of  $2\pi\gamma/W$  and  $2\pi\gamma/L$  for the nanoribbon and nanotubes, respectively, the peak intensities in these units can be compared by the peak heights. The peak intensities for the nanoribbon are about half of those for the nanotubes. The factor of two comes from the difference in the number of the valleys. Figure 9(b), which is plotted in a similar way to Fig. 9(a), shows results in doped cases with  $k = 0$  for perpendicular polarization, where the result for the nanoribbon is the same as that for  $\varepsilon_F(2\pi\gamma/L)^{-1} = 0.5$  in Fig. 6(c). The energy of the plasmon peak for the nanoribbon approximately agrees with those of the nanotubes while the peak intensity for the nanoribbon is about half or less of those for the nanotubes mainly because of the difference in the number of the valleys.

Figures 9(d) and 9(e) are similar plots to Figs. 9(a) and 9(b), respectively. In Figs. 9(d) and 9(e), the results of the armchair nanoribbon in Figs. 7(a) and 7(c), respectively, and those of the zigzag nanoribbon in Figs. 8(a) and 8(c), respectively, are shown. The results are similar to those of the semiconducting nanoribbon and nanotubes. In the case of metals, exact agreement of the energy bands between nanoribbons and nanotubes only exists for armchair nanoribbons. For zigzag nanoribbons, the energy bands  $v1$  and  $c1$  are

considerably different from the linear dispersions of metallic armchair nanoribbons and metallic nanotubes. In spite of this fact, the energy of the exciton peak of the zigzag nanoribbon in Fig. 9(d), which is associated with the energy bands  $v1$  and  $c2$ , approximately agrees with those of the armchair nanoribbon and the carbon nanotubes. This is because in zigzag nanoribbons, separation between the energy bands  $v1$  and  $c2$  for the wave vector at the bottom of the energy band  $c2$  is similar to that between the energy bands  $v2$  and  $c2$  of metallic armchair nanoribbons in units of  $2\pi\gamma/W$ .

Next we consider the plasmons caused by optical transitions within the same energy bands. Analytical expressions of energy dispersion relations of these plasmons can be obtained in the long-wavelength limit in the case of a single channel. We have for nanoribbons

$$\hbar\Omega_v = \gamma|k| \left( -\frac{2g_s}{\pi} \frac{e^2}{\kappa\gamma} \frac{\hbar v_F}{\gamma} \log \frac{|k|W}{2} \right)^{1/2}, \quad (36)$$

and for nanotubes

$$\hbar\Omega_v = \gamma|k| \left( -\frac{4g_s}{\pi} \frac{e^2}{\kappa\gamma} \frac{\hbar v_F}{\gamma} \log \frac{|k|L}{4\pi} \right)^{1/2}, \quad (37)$$

where  $v_F$  is the Fermi velocity. Equations (36) and (37) are derived in Appendix B. In the cases of metallic nanoribbons and metallic nanotubes, where  $v_F = \gamma/\hbar$ , Eqs. (36) and (37) become those obtained in earlier studies [27,52]. Thus, when the wave vector is scaled by  $1/W$  and  $2\pi/L$  for nanoribbons and nanotubes, respectively, and energy is scaled by  $(1/\sqrt{2})(\gamma/W)$  and  $2\pi\gamma/L$  for nanoribbons and nanotubes, respectively, the plasmon energy is the same between nanoribbons and nanotubes. The difference of  $2\pi$  in the scaling factors for the wave vector and energy comes from that in the geometry of the systems and the difference of  $1/\sqrt{2}$  in the scaling factor for energy arises from that in the number of the valleys. It should be noted that although zigzag nanoribbons have the two valleys, the lowest conduction or the highest valence bands at the  $K$  and  $K'$  points only contribute to a single channel as a whole because of their shapes.

In Figs. 9(c) and 9(f), peaks arising from these plasmons in optical absorption spectra for semiconductor and metal, respectively, are plotted in the above-mentioned units. Vertical solid and dashed lines denote the analytical plasmon energies for the armchair nanoribbons and nanotubes and for the zigzag nanoribbon, respectively. In each figure,  $v_F$  is the same between the armchair nanoribbon and nanotubes while in Fig. 9(f),  $v_F$  for the zigzag nanoribbon is slightly smaller than that for the others. Small deviations of the peak positions from the vertical solid and dashed lines come from effects of higher-order terms of the wave vector and those of the interactions  $v_{(r,t)(s,u)}^{(2)}$  neglected in Eqs. (36) and (37). The peak positions for the nanoribbons and nanotubes are approximately in agreement with each other while the intensities of the peaks for the nanoribbons are about half of those for the nanotubes because of the difference in the number of the valleys.

Dependences of the optical absorption spectra on the sizes of  $W$  and  $L$  for nanoribbons and nanotubes, respectively, originate from a cutoff energy of half the  $\pi$  band width in calculations of the electric susceptibility and the self-energy [7]. These dependences are gradual as shown in all the results

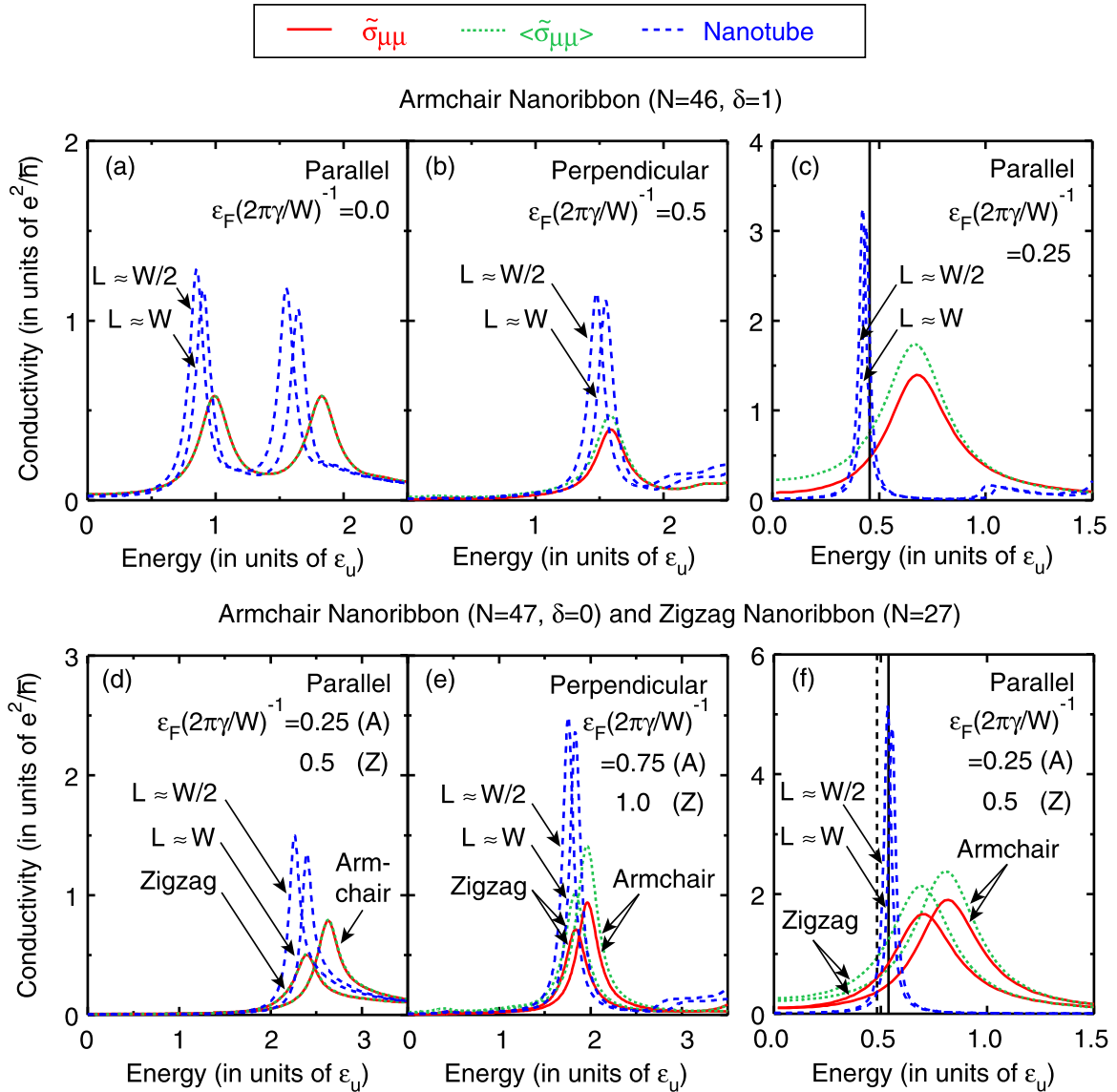


FIG. 9. Energy dependence of  $\text{Re}\tilde{\sigma}_{\mu\mu}$  (solid lines) and  $\text{Re}(\tilde{\sigma}_{\mu\mu})$  (dotted lines) for graphene nanoribbons and that of the real part of the dynamical conductivity for carbon nanotubes (dashed lines) for parallel polarization in (a), (c), (d), and (f) and for perpendicular polarization in (b) and (e). Units of the horizontal axes are  $\pi\gamma/W$  in (a), (b), (d), and (e) and  $(1/\sqrt{2})(\gamma/W)$  in (c) and (f) for the nanoribbons and  $2\pi\gamma/L$  for the nanotubes. In (a), (b), (d), and (e),  $\Gamma$  is 0.07 and in (c) and (f), 0.02 in units of  $2\pi\gamma/W$  and  $2\pi\gamma/L$  for the nanoribbons and nanotubes, respectively. For the nanotubes, results for  $L \approx W/2$  and  $W$  are shown. (a) Results for the  $N = 46$  armchair nanoribbon and semiconducting nanotubes for  $\varepsilon_F = 0$  and  $k = 0$ . (b) Results for the  $N = 46$  armchair nanoribbon with  $\varepsilon_F(2\pi\gamma/W)^{-1} = 0.5$  and semiconducting nanotubes with  $\varepsilon_F(2\pi\gamma/L)^{-1} = 1.0$  for  $k = 0$ . (c) Results for the  $N = 46$  armchair nanoribbon with  $\varepsilon_F(2\pi\gamma/W)^{-1} = 0.25$  and  $k(1/W)^{-1} = 0.232$  and semiconducting nanotubes with  $\varepsilon_F(2\pi\gamma/L)^{-1} = 0.5$  and  $k(2\pi/L)^{-1} = 0.232$ , where  $v_F(\gamma/\hbar)^{-1} = 0.745$ . A vertical solid line indicates an analytical plasmon energy. (d) Results for the  $N = 47$  armchair nanoribbon with  $\varepsilon_F(2\pi\gamma/W)^{-1} = 0.25$ , the  $N = 27$  zigzag nanoribbon with  $\varepsilon_F(2\pi\gamma/W)^{-1} = 0.5$ , and metallic nanotubes with  $\varepsilon_F(2\pi\gamma/L)^{-1} = 0.5$  for  $k = 0$ . (e) Results for the  $N = 47$  armchair nanoribbon with  $\varepsilon_F(2\pi\gamma/W)^{-1} = 0.75$ , the  $N = 27$  zigzag nanoribbon with  $\varepsilon_F(2\pi\gamma/W)^{-1} = 1.0$ , and metallic nanotubes with  $\varepsilon_F(2\pi\gamma/L)^{-1} = 1.0$  for  $k = 0$ . (f) Results for the  $N = 47$  armchair nanoribbon with  $\varepsilon_F(2\pi\gamma/W)^{-1} = 0.25$  and  $k(1/W)^{-1} = 0.237$ , the  $N = 27$  zigzag nanoribbon with  $\varepsilon_F(2\pi\gamma/W)^{-1} = 0.5$  and  $k(1/W)^{-1} = 0.235$ , and metallic nanotubes with  $\varepsilon_F(2\pi\gamma/L)^{-1} = 0.5$  and  $k(2\pi/L)^{-1} = 0.237$ , where  $v_F(\gamma/\hbar)^{-1} = 1.0$  for the armchair nanoribbon and nanotubes and 0.819 for the zigzag nanoribbon. Vertical solid and dashed lines indicate analytical plasmon energies for the armchair nanoribbon and nanotubes and for the zigzag nanoribbon, respectively.

of the nanotubes in Fig. 9. Thus, the correspondences between the nanoribbons and nanotubes in Fig. 9 are considered to be valid in a wide range of categories of nanoribbons and nanotubes.

We briefly consider asymptotic behaviors of the excitons and the plasmons in the limit of large width. First,

we consider a case where the Fermi energy is set to zero or a constant in units of  $2\pi\gamma/W$ . In this case, the excitons would diminish because energies of associated interband transitions vanish. The plasmons caused by intraband transitions would disappear because the electron density per unit area around the Fermi energy vanishes, and the plasmons

caused by interband transitions would also vanish because energy gaps above associated one-particle excitation continuums disappear. Another case in which the Fermi energy is fixed to a constant independent of the width may be more realistic. In this case, the excitons would disappear because separations between energy bands vanish and minima of energies for optical transitions with high joint densities of states like edges of parabolic energy bands vanish. The plasmons caused by intraband transitions would change to those in graphene since the electron density per unit area around the Fermi energy converges to a constant, while the plasmons caused by interband transitions would disappear because of the same reason as that in the first case. For high conduction and low valence bands, the average number of edges of energy bands in the energy interval  $2\pi\gamma/W$  is four both for armchair and zigzag nanoribbons. Thus, between armchair and zigzag nanoribbons with similar Fermi energies and similar widths, the densities of free electrons are approximately the same and the plasmons caused by intraband transitions would be less distinguishable, smearing the effects of the boundaries of nanoribbons.

Finally, we discuss methods to calculate optical absorption with depolarization effects. Although  $\tilde{\sigma}_{\mu\mu}$  in Eq. (34) gives accurate optical absorption spectra with depolarization effects, its calculation is complicated. On the other hand,  $\langle\tilde{\sigma}_{\mu\mu}\rangle$  in Eq. (35) can be simply calculated. In Fig. 9, dotted lines show  $\langle\tilde{\sigma}_{\mu\mu}\rangle$ , which corresponds to  $\tilde{\sigma}_{\mu\mu}$  denoted by the solid lines. For the exciton peaks in Figs. 9(a) and 9(d), almost no difference between  $\langle\tilde{\sigma}_{\mu\mu}\rangle$  and  $\tilde{\sigma}_{\mu\mu}$  can be seen because excitons for parallel polarization are hardly affected by depolarization effects [112]. For the plasmons in Figs. 9(b), 9(c), 9(e), and 9(f), peak positions for  $\langle\tilde{\sigma}_{\mu\mu}\rangle$  are almost the same as those for  $\tilde{\sigma}_{\mu\mu}$  while peak intensities for  $\langle\tilde{\sigma}_{\mu\mu}\rangle$  are slightly larger than those for  $\tilde{\sigma}_{\mu\mu}$  by factors of less than one half in the studied cases. Thus, this indicates that  $\langle\tilde{\sigma}_{\mu\mu}\rangle$  can semiquantitatively describe optical absorption spectra with depolarization effects.

The above result may be understood by optical absorption of systems with the continuous translational symmetry according to a theory by Ajiki and Ando [114,115]. In this case, the conductivities with and without depolarization effects,  $\tilde{\sigma}_{\mu\mu}(\mathbf{r}, \mathbf{r}')$  and  $\sigma_{\mu\mu}(\mathbf{r}, \mathbf{r}')$ , respectively, depend on  $\mathbf{r}$  and  $\mathbf{r}'$  as a function of  $\mathbf{r} - \mathbf{r}'$ . Since the integrals in Eqs. (32) for these conductivities become convolutions, for an external electric field  $E_{0,\mu}(\mathbf{k})$  with a wave vector  $\mathbf{k}$ , we have a self-consistent electric field  $E_{\mu}(\mathbf{k}) = [\tilde{\sigma}_{\mu\mu}(\mathbf{k})/\sigma_{\mu\mu}(\mathbf{k})]E_{0,\mu}(\mathbf{k})$ , where  $\tilde{\sigma}_{\mu\mu}(\mathbf{k})$  and  $\sigma_{\mu\mu}(\mathbf{k})$  are the Fourier transforms of  $\tilde{\sigma}_{\mu\mu}(\mathbf{r}, \mathbf{r}')$  and  $\sigma_{\mu\mu}(\mathbf{r}, \mathbf{r}')$ , respectively, with respect to  $\mathbf{r} - \mathbf{r}'$ . If we consider the conductivity with depolarization effects by calculating a self-consistent electric field using classical electrodynamics, we have

$$\tilde{\sigma}_{\mu\mu}(\mathbf{k}) = \frac{\sigma_{\mu\mu}(\mathbf{k})}{1 + i(k_{\mu}^2/\hat{\omega})V(\mathbf{k})\sigma_{\mu\mu}(\mathbf{k})}, \quad (38)$$

where the self-consistent electric field is derived from the continuity equation and the Poisson equation and  $V(\mathbf{k})$  is the Fourier transform of  $1/|\mathbf{r}|$  for the space of the electronic system. Thus we have optical absorption power per unit area given by

$$P = \frac{|E_{0,\mu}(\mathbf{k})|^2}{2(AW)^2} \text{Re}\tilde{\sigma}_{\mu\mu}(\mathbf{k}), \quad (39)$$

where we used that  $\sigma_{\mu\mu}(\mathbf{k})$  can approximately be regarded as real numbers at energies for peaks in optical absorption spectra. Optical absorption is simply characterized by the real part of the conductivity with depolarization effects. Thus, if  $\langle\tilde{\sigma}_{\mu\mu}\rangle$  in Eq. (35) is approximately regarded as the Fourier transform with zero wave vector in the direction of the width,  $\langle\tilde{\sigma}_{\mu\mu}\rangle$  may be expected to well describe optical absorption with depolarization effects for homogeneous external electric fields as long as the confinement does not have severe effects.

## V. SUMMARY AND CONCLUSIONS

In conclusion, we have theoretically studied the optical response of armchair and zigzag graphene nanoribbons without and with doping in an effective-mass approximation by including electron correlations in the RPA. For screening of the Coulomb interactions, antiscreening effects locally appear in semiconducting armchair nanoribbons. In optical absorption spectra, various prominent peaks arise from excitons and plasmons, which can be assigned to specific optical transitions. For parallel polarization, exciton peaks at high energies split in armchair nanoribbons because of interactions with dark excitons. For perpendicular polarization, in nondoped semiconducting armchair nanoribbons, moderate exciton peaks appear while in doped armchair and zigzag nanoribbons, only when the Fermi energy crosses at least two energy bands, plasmon peaks appear because of a nature of Dirac electrons. Energy and intensity of optical absorption peaks arising from the excitons and plasmons in a wide range of categories of nanoribbons approximately correspond to those of carbon nanotubes with a factor of about two in intensity by appropriate scaling of energy and the wave vector. The numerical results indicate that the dynamical conductivity calculated with the use of electronic states in the RPA can semiquantitatively describe optical absorption spectra with depolarization effects by itself.

## ACKNOWLEDGMENTS

This work was supported by Japan Society for the Promotion of Science KAKENHI Grant No. JP20K03799. The numerical calculations were partly performed at Cyberscience Center, Tohoku University.

## APPENDIX A: DERIVATION OF THE SELECTION RULE

We derive the selection rule for optical transitions in nanoribbons without electron correlations and depolarization effects. In this case, the selection rule is determined by  $\langle\tilde{\sigma}_{\mu\mu}\rangle$  with velocity matrix elements between electron states and hole ones in the one-particle model. The velocity operator is  $v_{\mu}(w; k) = (\gamma/\hbar)\sigma_{\mu}e^{-ik\hat{l}}\delta(w - \hat{w})$  and  $(\gamma/\hbar)\sigma_{\mu}^*e^{-ik\hat{l}}\delta(w - \hat{w})$  for the  $K$  and  $K'$  points, respectively, where  $\hat{w}$  and  $\hat{l}$  are position operators in the directions of the width and length, respectively.

For armchair nanoribbons, we denote one-particle states by  $|s_e, \mathbf{k}, i\rangle$  with  $i = \{1, 2\}$ , where  $i$  indicates  $C_i$  in Eq. (12), except for states with  $k_x = 0$  in the linear dispersions of metallic nanoribbons, which we denote as  $|s_e, k_y, 0\rangle$ , where 0 indicates  $C_0$  in Eq. (14). For parallel polarization, velocity

matrix elements are given by

$$\langle\langle s_e, \mathbf{k}, 1 | \hat{v}_y | s'_e, \mathbf{k}', 1 \rangle\rangle = \frac{i\gamma}{2\hbar} (s'_e e^{i\varphi} - s_e e^{-i\varphi}) f_{y,-}, \quad (\text{A1})$$

$$\langle\langle s_e, \mathbf{k}, 1 | \hat{v}_y | s'_e, \mathbf{k}', 2 \rangle\rangle = \frac{i\gamma}{2\hbar} (s'_e e^{i\varphi} + s_e e^{i\varphi'}) f_{y,+}, \quad (\text{A2})$$

$$\langle\langle s_e, \mathbf{k}, 2 | \hat{v}_y | s'_e, \mathbf{k}', 2 \rangle\rangle = -\frac{i\gamma}{2\hbar} (s'_e e^{-i\varphi} - s_e e^{i\varphi'}) f_{y,-}, \quad (\text{A3})$$

with

$$f_{y,\pm} = \frac{\sin[(k_x \pm k'_x)W]}{(k_x \pm k'_x)W}, \quad (\text{A4})$$

where we define  $\langle\langle \dots | \hat{v}_\mu | \dots \rangle\rangle = (1/W) \int_0^W d w \langle \dots | \hat{v}_\mu(w; k) | \dots \rangle$  and  $e^{i\varphi}$  is  $e^{i\varphi}$  with replacement  $\mathbf{k} \rightarrow \mathbf{k}'$ . The first and the third matrix elements are valid for  $k_x \neq k'_x$  and are those with  $f_{y,-} \rightarrow 1$  for  $k_x = k'_x$ . For metallic nanoribbons, in particular, since  $k_x, k'_x = m\pi/W$  in Eq. (11) and  $f_{y,\pm} = 0$ , only  $\langle\langle s_e, \mathbf{k}, i | \hat{v}_y | s'_e, \mathbf{k}', i \rangle\rangle$  with  $i = \{1, 2\}$  for  $k_x = k'_x$  can be nonzero. For transitions associated with the linear dispersions, we have

$$\langle\langle s_e, k_y, 0 | \hat{v}_x | s'_e, \mathbf{k}', i \rangle\rangle = 0 \quad (\text{A5})$$

$$\langle\langle s_e, k_y, 0 | \hat{v}_y | s'_e, k'_y, 0 \rangle\rangle = -\frac{\gamma}{2\hbar} (s'_e \text{sgn} k_y + s_e \text{sgn} k'_y), \quad (\text{A6})$$

where  $i = \{1, 2\}$ .

We consider optical transitions between band edges at  $k_y = k'_y = 0$ . In this case,  $e^{\pm i\varphi} = \text{sgn} k_x = 1$ , where  $\text{sgn} k_x$  is the sign of  $k_x$ . In semiconducting nanoribbons, for transitions between the valence and conduction bands with  $s_e = -s'_e$ , those between energy bands with  $vi$  and  $ci$  are allowed, where we used  $f_{y,-} = 0$  in Eqs. (A1) and (A3) for  $k_x \neq k'_x$  because  $k_x - k'_x = n\pi/W$  with  $n$  being integers. The other transitions are prohibited. For intravalence band and intraconduction band transitions, there are no allowed transitions, where we used  $f_{y,+} = 0$  in Eq. (A2) because  $k_x + k'_x = n\pi/W$ . In metallic nanoribbons, only transitions between valence and conduction bands with  $vi$  and  $ci$ , respectively, where  $i \neq 1$  are allowed.

For perpendicular polarization, we have the following matrix elements:

$$\langle\langle s_e, \mathbf{k}, 1 | \hat{v}_x | s'_e, \mathbf{k}', 1 \rangle\rangle = \frac{i\gamma}{2\hbar} (s'_e e^{i\varphi} + s_e e^{-i\varphi'}) f_{x,-}, \quad (\text{A7})$$

$$\langle\langle s_e, \mathbf{k}, 1 | \hat{v}_x | s'_e, \mathbf{k}', 2 \rangle\rangle = \frac{i\gamma}{2\hbar} (s'_e e^{i\varphi} - s_e e^{i\varphi'}) f_{x,+}, \quad (\text{A8})$$

$$\langle\langle s_e, \mathbf{k}, 2 | \hat{v}_x | s'_e, \mathbf{k}', 2 \rangle\rangle = \frac{i\gamma}{2\hbar} (s'_e e^{-i\varphi} + s_e e^{i\varphi'}) f_{x,-}, \quad (\text{A9})$$

with

$$f_{x,\pm} = \frac{\cos[(k_x \pm k'_x)W] - 1}{(k_x \pm k'_x)W}. \quad (\text{A10})$$

The first and the third matrix elements are valid for  $k_x \neq k'_x$  and vanish for  $k_x = k'_x$ . We also have matrix elements associated with the linear dispersions of metallic nanoribbons as

$$\begin{aligned} &\langle\langle s_e, k_y, 0 | \hat{v}_x | s'_e, \mathbf{k}', 1 \rangle\rangle \\ &= -\langle\langle s_e, k_y, 0 | \hat{v}_x | s'_e, \mathbf{k}', 2 \rangle\rangle \\ &= -\frac{i\gamma}{2\hbar} (i s'_e \text{sgn} k_y + s_e e^{-i\varphi'}) \frac{\cos k'_x W - 1}{k'_x W}, \end{aligned} \quad (\text{A11})$$

$$\langle\langle s_e, k_y, 0 | \hat{v}_x | s'_e, k'_y, 0 \rangle\rangle = 0. \quad (\text{A12})$$

For transitions between band edges, we have the following selection rule: In semiconducting nanoribbons, transitions are allowed between the valence and conduction bands for the different  $C_i$ , i.e.,  $vi$  and  $cj$  with even  $i$  and odd  $j$  and with odd  $i$  and even  $j$ , while intravalence (intraconduction) band transitions are allowed between energy bands for the same  $C_i$ , i.e.,  $vi$  and  $vj$  ( $ci$  and  $cj$ ) with even  $i$  and even  $j$  and with odd  $i$  and odd  $j$ , except for the case of  $k_x - k'_x = 2n\pi/W$  with  $n$  being integers. In metallic nanoribbons, the same rule as that for semiconducting nanoribbons is applicable except that transitions from the Dirac point to the other energy bands with  $k'_x \neq 2n\pi/W$  can be allowed by taking either of the limits of  $k_y \rightarrow \pm 0$ .

For zigzag nanoribbons, we denote one-particle states other than edge states as  $|v, s_e, \mathbf{k}\rangle$ . Velocity matrix elements between these states at the  $K$  point are given by

$$\begin{aligned} \langle\langle K, s_e, \mathbf{k} | \hat{v}_\mu | K, s'_e, \mathbf{k}' \rangle\rangle &= \frac{2\gamma C_z^2}{\hbar} \frac{-k_y \sin k'_y W + k'_y \sin k_y W}{k_y^2 - (k'_y)^2} \\ &\times g_1(k_y, k'_y), \end{aligned} \quad (\text{A13})$$

with

$$g_1(k_y, k'_y) = \begin{cases} s'_e \text{sgn}(\sin k_y W) + s_e \text{sgn}(\sin k'_y W) & \text{for } \mu = x \\ i[-s'_e \text{sgn}(\sin k_y W) + s_e \text{sgn}(\sin k'_y W)] & \text{for } \mu = y, \end{cases} \quad (\text{A14})$$

where  $k_x$  and  $k'_x$  are eliminated by using Eq. (18). For transitions associated with edge states, which we denote as  $|K, s_e, \tilde{\mathbf{k}}\rangle$  with  $\tilde{\mathbf{k}} = (k_x, \tilde{k}_y)$ , velocity matrix elements are given by

$$\langle\langle K, s_e, \tilde{\mathbf{k}} | \hat{v}_\mu | K, s'_e, \mathbf{k}' \rangle\rangle = \frac{2\sqrt{2}\gamma C_z \tilde{C}_z}{\hbar} \frac{-\tilde{k}_y \sin k'_y W + k'_y \sinh \tilde{k}_y W}{\tilde{k}_y^2 + (k'_y)^2} g_2(k'_y), \quad (\text{A15})$$

$$\langle\langle K, s_e, \tilde{\mathbf{k}} | \hat{v}_\mu | K, s'_e, \tilde{\mathbf{k}}' \rangle\rangle = \frac{4\gamma \tilde{C}_z^2}{\hbar} \frac{-\tilde{k}_y \sinh \tilde{k}'_y W + \tilde{k}'_y \sinh \tilde{k}_y W}{\tilde{k}_y^2 - (\tilde{k}'_y)^2} g_3, \quad (\text{A16})$$

with  $\tilde{C}_z$  being a normalization factor for edge states and

$$g_2(k'_y) = \begin{cases} i[s'_e + s_e \text{sgn}(\sin k'_y W)] & \text{for } \mu = x \\ s'_e - s_e \text{sgn}(\sin k'_y W) & \text{for } \mu = y, \end{cases} \quad (\text{A17})$$

$$g_3 = \begin{cases} -s'_e - s_e & \text{for } \mu = x \\ i(s'_e - s_e) & \text{for } \mu = y. \end{cases} \quad (\text{A18})$$

From Eq. (18),  $k_y$  for the  $i$ th valence and conduction bands satisfies  $(i-1)\pi/W < k_y < i\pi/W$ . Thus, for parallel polarization with  $\mu = x$ , transitions between the valence and conduction bands with  $vi$  and  $cj$ , respectively, are allowed for odd (even)  $i$  and even (odd)  $j$  while intravalence (intraconduction) band transitions between  $vi$  and  $vj$  ( $ci$  and  $cj$ ) are allowed for odd  $i$  and odd  $j$  and for even  $i$  and even  $j$ . For perpendicular polarization with  $\mu = y$ , a selection rule is that for parallel polarization where the rule for band indices  $i$  and  $j$  for transitions between the valence and conduction bands is exchanged with that for intravalence band and intraconduction band transitions. For the  $K'$  point, we have the same selection rule.

## APPENDIX B: ENERGY DISPERSION RELATIONS OF PLASMONS

We consider plasmons for transitions in the same energy bands in the long-wavelength limit in the case of a single channel. When  $v_{(r;i)(s;u)}^{(2)}$  is neglected in the RPA equation, the RPA equation is written as [59,111,112]

$$g_s \left( \sum_{\langle m',i' \rangle} v_{(m;i)(i';m')}^{(1)} X_{m'i'} + \sum_{\langle m',i' \rangle} v_{(m;i)(m';i')}^{(1)} Y_{m'i'} \right) = (\hbar\Omega_v - \varepsilon_m + \varepsilon_i) X_{mi}, \quad (\text{B1})$$

$$-g_s \left( \sum_{\langle m',i' \rangle} v_{(m;i)(m';i')}^{(1)*} X_{m'i'} + \sum_{\langle m',i' \rangle} v_{(m;i)(i';m')}^{(1)*} Y_{m'i'} \right) = (\hbar\Omega_v + \varepsilon_m - \varepsilon_i) Y_{mi}, \quad (\text{B2})$$

where  $m$  and  $m'$  denote electron states,  $i$  and  $i'$  indicate hole ones, and the summations run over e-h pairs for the corresponding expansion coefficients. Electron and hole states for  $Y_{mi}$  are chosen in such a way that  $k_m - k_i$  for  $Y_{mi}$  is  $k_m - k_i$  for

$X_{mi}$  with the minus sign. In the long-wavelength limit, since the plasmons consist of e-h pairs in the same energy band  $c1$  or  $v1$  with infinitesimally small separation in the wave vector, we have

$$v_{(m;i)(i';m')}^{(1)} = v_{(m;i)(m';i')}^{(1)} = -\frac{2e^2}{\kappa A} \log \frac{|k|W}{2}, \quad (\text{B3})$$

where  $\mathbf{F}_m^\dagger(w)\mathbf{F}_i(w) \approx \mathbf{F}_i^\dagger(w)\mathbf{F}_m(w) \approx 1/W$  was used and  $|k| = |k_m - k_i| = |k_{m'} - k_{i'}| \ll 2\pi/W$ . Substituting Eq. (B3) into Eqs. (B1) and (B2), we have

$$X_{mi} = -\frac{2e^2}{\kappa A} \log \frac{|k|W}{2} \frac{C}{\hbar\Omega_v - \varepsilon_m + \varepsilon_i}, \quad (\text{B4})$$

$$Y_{mi} = \frac{2e^2}{\kappa A} \log \frac{|k|W}{2} \frac{C}{\hbar\Omega_v + \varepsilon_m - \varepsilon_i}, \quad (\text{B5})$$

with

$$C = \sum_{\langle m,i \rangle} X_{mi} + \sum_{\langle m,i \rangle} Y_{mi}. \quad (\text{B6})$$

Substituting Eqs. (B4) and (B5) into Eq. (B6), we have

$$1 + \frac{2e^2 g_s}{\kappa A} \log \frac{|k|W}{2} \sum_{\langle m,i \rangle} \frac{2(\varepsilon_m - \varepsilon_i)}{(\hbar\Omega_v)^2 - (\varepsilon_m - \varepsilon_i)^2} = 0, \quad (\text{B7})$$

where the summation runs over e-h pairs for  $X_{mi}$ . Using  $\varepsilon_m - \varepsilon_i \approx \hbar v_F |k|$  and that the number of e-h pairs contributing in the summation is given by  $|k|(2\pi/A)^{-1}$ , we have Eq. (36). In the case of carbon nanotubes, replacing Eq. (B3) with [59,112]

$$v_{(m;i)(i';m')}^{(1)} = v_{(m;i)(m';i')}^{(1)} = -\frac{2e^2}{\kappa A} \log \frac{|k|L}{4\pi}, \quad (\text{B8})$$

which is given from matrix elements of the Coulomb interactions for nanotubes [7], and adding a factor of two of the valley degeneracy in front of the summation in Eq. (B7), we have Eq. (37).

- 
- [1] M. Fujita, K. Wakabayashi, K. Nakada, and K. Kusakabe, *J. Phys. Soc. Jpn.* **65**, 1920 (1996).  
[2] K. Nakada, M. Fujita, G. Dresselhaus, and M. S. Dresselhaus, *Phys. Rev. B* **54**, 17954 (1996).  
[3] K. Wakabayashi, M. Sigrist, and M. Fujita, *J. Phys. Soc. Jpn.* **67**, 2089 (1998).  
[4] K. Wakabayashi, M. Fujita, H. Ajiki, and M. Sigrist, *Phys. Rev. B* **59**, 8271 (1999).  
[5] Y.-W. Son, M. L. Cohen, and S. G. Louie, *Nature (London)* **444**, 347 (2006).  
[6] Y.-W. Son, M. L. Cohen, and S. G. Louie, *Phys. Rev. Lett.* **97**, 216803 (2006).  
[7] T. Ando, *J. Phys. Soc. Jpn.* **66**, 1066 (1997).  
[8] C. D. Spataru, S. Ismail-Beigi, L. X. Benedict, and S. G. Louie, *Phys. Rev. Lett.* **92**, 077402 (2004).  
[9] E. Chang, G. Bussi, A. Ruini, and E. Molinari, *Phys. Rev. Lett.* **92**, 196401 (2004).  
[10] V. Perebeinos, J. Tersoff, and Ph. Avouris, *Phys. Rev. Lett.* **92**, 257402 (2004).  
[11] H. Zhao and S. Mazumdar, *Phys. Rev. Lett.* **93**, 157402 (2004).  
[12] C. L. Kane and E. J. Mele, *Phys. Rev. Lett.* **93**, 197402 (2004).  
[13] M. Ichida, S. Mizuno, Y. Tani, Y. Saito, and A. Nakamura, *J. Phys. Soc. Jpn.* **68**, 3131 (1999).  
[14] S. M. Bachilo, M. S. Strano, C. Kittrell, R. H. Hauge, R. E. Smalley, and R. B. Weisman, *Science* **298**, 2361 (2002).  
[15] F. Wang, G. Dukovic, L. E. Brus, and T. F. Heinz, *Science* **308**, 838 (2005).  
[16] Y. Wang, K. Kempa, B. Kimball, J. B. Carlson, G. Benham, W. Z. Li, T. Kempa, J. Rybczynski, A. Herczynski, and Z. F. Ren, *Appl. Phys. Lett.* **85**, 2607 (2004).  
[17] N. Akima, Y. Iwasa, S. Brown, A. M. Barbour, J. Cao, J. L. Musfeldt, H. Matsui, N. Toyota, M. Shiraishi, H. Shimoda, and O. Zhou, *Adv. Mater.* **18**, 1166 (2006).  
[18] M. V. Shuba, A. G. Paddubskaya, A. O. Plyushch, P. P. Kuzhir, G. Ya. Slepyan, S. A. Maksimenko, V. K. Ksenevich, P. Buka, D. Seliuta, I. Kasalynas, J. Macutkevicius, G. Valusis, C. Thomsen, and A. Lakhtakia, *Phys. Rev. B* **85**, 165435 (2012).  
[19] Q. Zhang, E. H. H aroz, Z. Jin, L. Ren, X. Wang, R. S. Arvidson, A. L uttge, and J. Kono, *Nano Lett.* **13**, 5991 (2013).

- [20] L. Ren, Q. Zhang, C. L. Pint, A. K. Wójcik, M. Bunney, Jr., T. Arikawa, I. Kawayama, M. Tonouchi, R. H. Hauge, A. A. Belyanin, and J. Kono, *Phys. Rev. B* **87**, 161401(R) (2013).
- [21] T. Morimoto, S.-K. Joung, T. Saito, D. N. Futaba, K. Hata, and T. Okazaki, *ACS Nano* **8**, 9897 (2014).
- [22] T. Morimoto, M. Ichida, Y. Ikemoto, and T. Okazaki, *Phys. Rev. B* **93**, 195409 (2016).
- [23] X. He, W. Gao, L. Xie, B. Li, Q. Zhang, S. Lei, J. M. Robinson, E. H. Hároz, S. K. Doorn, W. Wang, R. Vajtai, P. M. Ajayan, W. Wade Adams, R. H. Hauge, and J. Kono, *Nat. Nanotechnol.* **11**, 633 (2016).
- [24] P. Karlsen, M. V. Shuba, C. Beckerleg, D. I. Yuko, P. P. Kuzhir, S. A. Maksimenko, V. Ksenevich, H. Viet, A. G. Nasibulin, R. Tenne, and E. Hendry, *J. Phys. D: Appl. Phys.* **51**, 014003 (2018).
- [25] G. Ya. Slepyan, S. A. Maksimenko, A. Lakhtakia, O. Yevtushenko, and A. V. Gusakov, *Phys. Rev. B* **60**, 17136 (1999).
- [26] J. Hao and G. W. Hanson, *Phys. Rev. B* **74**, 035119 (2006).
- [27] T. Nakanishi and T. Ando, *J. Phys. Soc. Jpn.* **78**, 114708 (2009).
- [28] G. Ya. Slepyan, M. V. Shuba, S. A. Maksimenko, C. Thomsen, and A. Lakhtakia, *Phys. Rev. B* **81**, 205423 (2010).
- [29] M.-F. Lin and F.-L. Shyu, *J. Phys. Soc. Jpn.* **69**, 3529 (2000).
- [30] V. Barone, O. Hod, and G. E. Scuseria, *Nano Lett.* **6**, 2748 (2006).
- [31] H. Hsu and L. E. Reichl, *Phys. Rev. B* **76**, 045418 (2007).
- [32] E. Ahmadi and A. Asgari, *Procedia Eng.* **8**, 25 (2011).
- [33] H. C. Chung, M. H. Lee, C. P. Chang, and M. F. Lin, *Opt. Express* **19**, 23350 (2011).
- [34] K. Gundra and A. Shukla, *Phys. Rev. B* **83**, 075413 (2011).
- [35] K.-I. Sasaki, K. Kato, Y. Tokura, K. Oguri, and T. Sogawa, *Phys. Rev. B* **84**, 085458 (2011).
- [36] V. A. Saroka, M. V. Shuba, and M. E. Portnoi, *Phys. Rev. B* **95**, 155438 (2017).
- [37] V. A. Saroka, A. L. Pushkarchuk, S. A. Kuten, and M. E. Portnoi, *J. of Saudi Chem. Soc.* **22**, 985 (2018).
- [38] R. B. Payod, D. Grassano, G. Nonato C. Santos, D. I. Levshov, O. Pulci, and V. A. Saroka, *Nat. Commun.* **11**, 82 (2020).
- [39] L. Yang, M. L. Cohen, and S. G. Louie, *Nano Lett.* **7**, 3112 (2007).
- [40] L. Yang, M. L. Cohen, and S. G. Louie, *Phys. Rev. Lett.* **101**, 186401 (2008).
- [41] D. Prezzi, D. Varsano, A. Ruini, A. Marini, and E. Molinari, *Phys. Rev. B* **77**, 041404(R) (2008).
- [42] Y. L. Jia, X. Geng, H. Sun, and Y. Luo, *Eur. Phys. J. B* **83**, 451 (2011).
- [43] X. Zhu and H. Su, *J. Phys. Chem. A* **115**, 11998 (2011).
- [44] Y. Lu, S. Zhao, W. Lu, H. Liu, and W. Liang, *J. Appl. Phys.* **115**, 103701 (2014).
- [45] B. S. Monozon and P. Schmelcher, *Physica B (Amsterdam)* **500**, 89 (2016).
- [46] R. Denk, M. Hohage, P. Zeppenfeld, J. Cai, C. A. Pignedoli, H. Söde, R. Fasel, X. Feng, K. Müllen, S. Wang, D. Prezzi, A. Ferretti, A. Ruini, E. Molinari, and P. Ruffieux, *Nat. Commun.* **5**, 4253 (2014).
- [47] A. Tries, S. Osella, P. Zhang, F. Xu, C. Ramanan, M. Kläui, Y. Mai, D. Beljonne, and H. I. Wang, *Nano Lett.* **20**, 2993 (2020).
- [48] L. Brey and H. A. Fertig, *Phys. Rev. B* **75**, 125434 (2007).
- [49] D. R. Andersen and H. Raza, *Phys. Rev. B* **85**, 075425 (2012).
- [50] W. Wang and J. M. Kinaret, *Phys. Rev. B* **87**, 195424 (2013).
- [51] C. E. P. Villegas, M. R. S. Tavares, G.-Q. Hai, and P. Vasilopoulos, *Phys. Rev. B* **88**, 165426 (2013).
- [52] A. A. Shylau, S. M. Badalyan, F. M. Peeters, and A. P. Jauho, *Phys. Rev. B* **91**, 205444 (2015).
- [53] M. S. Ukhtary, M. Maruoka, and R. Saito, *Phys. Rev. B* **100**, 155432 (2019).
- [54] D. Rodrigo, O. Limaj, D. Janner, D. Etezadi, F. J. García de Abajo, V. Pruneri, and H. Altug, *Science* **349**, 165 (2015).
- [55] H. Hu, X. Yang, F. Zhai, D. Hu, R. Liu, K. Liu, Z. Sun, and Q. Dai, *Nat. Commun.* **7**, 12334 (2016).
- [56] H. Hu, X. Yang, X. Guo, K. Khaliji, S. R. Biswas, F. J. García de Abajo, T. Low, Z. Sun, and Q. Dai, *Nat. Commun.* **10**, 1131 (2019).
- [57] J. Christensen, A. Manjavacas, S. Thongrattanasiri, F. H. L. Koppens, and F. J. García de Abajo, *ACS Nano* **6**, 431 (2012).
- [58] T. Igarashi, H. Kawai, K. Yanagi, N. T. Cuong, S. Okada, and T. Pichler, *Phys. Rev. Lett.* **114**, 176807 (2015).
- [59] S. Uryu, *Phys. Rev. B* **97**, 125420 (2018).
- [60] K. Yanagi, R. Okada, Y. Ichinose, Y. Yomogida, F. Katsutani, W. Gao, and J. Kono, *Nat. Commun.* **9**, 1121 (2018).
- [61] K.-I. Sasaki and Y. Tokura, *Phys. Rev. Appl.* **9**, 034018 (2018).
- [62] D. Satco, A. R. T. Nugraha, M. S. Ukhtary, D. Kopylova, A. G. Nasibulin, and R. Saito, *Phys. Rev. B* **99**, 075403 (2019).
- [63] C. T. White, J. Li, D. Gunlycke, and J. W. Mintmire, *Nano Lett.* **7**, 825 (2007).
- [64] L. Brey and H. A. Fertig, *Phys. Rev. B* **73**, 235411 (2006).
- [65] H. Ajiki and T. Ando, *J. Phys. Soc. Jpn.* **62**, 1255 (1993).
- [66] T. Tanaka, A. Tajima, R. Moriizumi, M. Hosoda, R. Ohno, E. Rokuta, C. Oshima, and S. Otani, *Solid State Commun.* **123**, 33 (2002).
- [67] Z. Chen, Y.-M. Lin, M. J. Rooks, and Ph. Avouris, *Physica E* **40**, 228 (2007).
- [68] M. Y. Han, B. Özyilmaz, Y. Zhang, and P. Kim, *Phys. Rev. Lett.* **98**, 206805 (2007).
- [69] X. Li, X. Wang, L. Zhang, S. Lee, and H. Dai, *Science* **319**, 1229 (2008).
- [70] L. Tapasztó, G. Dobrik, P. Lambin, and L. P. Biro, *Nat. Nanotechnol.* **3**, 397 (2008).
- [71] X. Jia, M. Hofmann, V. Meunier, B. G. Sumpter, J. Campos-Delgado, J. M. Romo-Herrera, H. Son, Y.-P. Hsieh, A. Reina, J. Kong, M. Terrones, and M. S. Dresselhaus, *Science* **323**, 1701 (2009).
- [72] A. L. Elías, A. R. Botello-Méndez, D. Meneses-Rodríguez, V. J. González, D. Ramírez-González, L. Ci, E. Muñoz-Sandoval, P. M. Ajayan, H. Terrones, and M. Terrones, *Nano Lett.* **10**, 366 (2010).
- [73] A. Kimouche, M. M. Ervasti, R. Drost, S. Halonen, A. Harju, P. M. Joensuu, J. Sainio, and P. Liljeroth, *Nat. Commun.* **6**, 10177 (2015).
- [74] G. D. Nguyen, F. M. Toma, T. Cao, Z. Pedramrazi, C. Chen, D. J. Rizzo, T. Joshi, C. Bronner, Y.-C. Chen, M. Favaro, S. G. Louie, F. R. Fischer, and M. F. Crommie, *J. Phys. Chem. C* **120**, 2684 (2016).
- [75] P. Ruffieux, S. Wang, B. Yang, C. Sánchez-Sánchez, J. Liu, T. Dienel, L. Talirz, P. Shinde, C. A. Pignedoli, D. Passerone, T. Dumslaff, X. Feng, K. Müllen, and R. Fasel, *Nature (London)* **531**, 489 (2016).

- [76] S. Iijima and T. Ichihashi, *Nature (London)* **363**, 603 (1993).
- [77] D. S. Bethune, C. H. Kiang, M. S. Devries, G. Gorman, R. Savoy, J. Vazquez, and R. Beyers, *Nature (London)* **363**, 605 (1993).
- [78] T. Guo, P. Nikolaev, A. Thess, D. T. Colbert, and R. E. Smalley, *Chem. Phys. Lett.* **243**, 49 (1995).
- [79] H. Dai, A. G. Rinzler, P. Nikolaev, A. Thess, D. T. Colbert, and R. E. Smalley, *Chem. Phys. Lett.* **260**, 471 (1996).
- [80] A. Thess, R. Lee, P. Nikolaev, H. Dai, P. Pettit, J. Robert, C. Xu, Y. H. Lee, S. G. Kim, A. G. Rinzler, D. T. Colbert, G. E. Scuseria, D. Tománek, J. E. Fischer, and R. E. Smalley, *Science* **273**, 483 (1996).
- [81] C. Journet, W. K. Maser, P. Bernier, A. Loiseau, M. Lamyde la Chapelle, S. Lefrant, P. Deniard, R. Lee, and J. E. Fischer, *Nature (London)* **388**, 756 (1997).
- [82] P. Nikolaev, M. J. Bronikowski, R. K. Bradley, F. Rohmund, D. T. Colbert, K. A. Smith, and R. E. Smalley, *Chem. Phys. Lett.* **313**, 91 (1999).
- [83] B. Kitiyanan, W. E. Alvarez, J. H. Harwell, and D. E. Resasco, *Chem. Phys. Lett.* **317**, 497 (2000).
- [84] M. J. Bronikowski, P. A. Willis, D. T. Colbert, K. A. Smith, and R. E. Smalley, *J. Vac. Sci. Technol. A* **19**, 1800 (2001).
- [85] S. Maruyama, R. Kojima, Y. Miyauchi, S. Chiashi, and M. Kohno, *Chem. Phys. Lett.* **360**, 229 (2002).
- [86] Y. Murakami, Y. Miyauchi, S. Chiashi, and S. Maruyama, *Chem. Phys. Lett.* **374**, 53 (2003).
- [87] T. Ando, *J. Phys. Soc. Jpn.* **74**, 777 (2005).
- [88] J. C. Slonczewski and P. R. Weiss, *Phys. Rev.* **109**, 272 (1958).
- [89] T. Nakanishi, M. Koshino, and T. Ando, *Phys. Rev. B* **82**, 125428 (2010).
- [90] H. Hadipour, E. Şaşıoğlu, F. Bagherpour, C. Friedrich, S. Blügel, and I. Mertig, *Phys. Rev. B* **98**, 205123 (2018).
- [91] T. Ando, *J. Phys. Soc. Jpn.* **73**, 3351 (2004).
- [92] S. Uryu, H. Ajiki, and T. Ando, *Phys. Rev. B* **78**, 115414 (2008).
- [93] T. Ando, *J. Phys. Soc. Jpn.* **78**, 104703 (2009).
- [94] S. Uryu and T. Ando, *Phys. Rev. B* **83**, 085404 (2011).
- [95] S. Uryu and T. Ando, *Phys. Rev. B* **86**, 125412 (2012).
- [96] T. Ando, *J. Phys. Soc. Jpn.* **75**, 074716 (2006).
- [97] P. Ring and P. Schuck, *The Nuclear Many-Body Problem* (Springer-Verlag, New York, 1980), and references therein.
- [98] A. Fetter and J. D. Walecka, *Quantum Theory of Many Particle Systems* (Dover, New York, 2003), and references therein.
- [99] S. Uryu and T. Ando, *Phys. Rev. B* **74**, 155411 (2006).
- [100] S. Uryu and T. Ando, *J. Phys.: Conf. Ser.* **302**, 012004 (2011).
- [101] H. Ajiki, *J. Phys. Soc. Jpn.* **82**, 054701 (2013).
- [102] L. J. Sham and T. M. Rice, *Phys. Rev.* **144**, 708 (1966).
- [103] R. Zimmermann, *Phys. Stat. Sol. B* **48**, 603 (1971).
- [104] G. Strinati, *Phys. Rev. Lett.* **49**, 1519 (1982).
- [105] G. Strinati, *Phys. Rev. B* **29**, 5718 (1984).
- [106] G. Onida, L. Reining, R. W. Godby, R. Del Sole, and W. Andreoni, *Phys. Rev. Lett.* **75**, 818 (1995).
- [107] S. Albrecht, G. Onida, and L. Reining, *Phys. Rev. B* **55**, 10278 (1997).
- [108] M. Rohlfing and S. G. Louie, *Phys. Rev. Lett.* **80**, 3320 (1998).
- [109] M. Rohlfing and S. G. Louie, *Phys. Rev. B* **62**, 4927 (2000).
- [110] L. X. Benedict, E. L. Shirley, and R. B. Bohn, *Phys. Rev. Lett.* **80**, 4514 (1998).
- [111] S. Uryu, *Phys. Rev. B* **94**, 155451 (2016); **96**, 199906(E) (2017).
- [112] S. Uryu, *Phys. Rev. B* **97**, 235413 (2018).
- [113] R. Kubo, *J. Phys. Soc. Jpn.* **12**, 570 (1957).
- [114] H. Ajiki and T. Ando, *Phys. B (Amsterdam)* **201**, 349 (1994).
- [115] H. Ajiki and T. Ando, *Jpn. J. Appl. Phys. Suppl.* **34-1**, 107 (1995).
- [116] S. Uryu, H. Ajiki, and H. Ishihara, *Phys. Rev. Lett.* **110**, 257401 (2013).
- [117] M. W. Graham, Y.-Z. Ma, A. A. Green, M. C. Hersam, and G. R. Fleming, *J. Chem. Phys.* **134**, 034504 (2011).
- [118] K. Matsuda, T. Inoue, Y. Murakami, S. Maruyama, and Y. Kanemitsu, *Phys. Rev. B* **77**, 033406 (2008).
- [119] K. Yoshikawa, R. Matsunaga, K. Matsuda, and Y. Kanemitsu, *Appl. Phys. Lett.* **94**, 093109 (2009).
- [120] D. T. Nguyen, C. Voisin, Ph. Roussignol, C. Roquelet, J. S. Lauret, and G. Cassabois, *Phys. Rev. B* **84**, 115463 (2011).
- [121] Y. Fujimoto and S. Uryu, *Phys. Rev. B* **88**, 235408 (2013).
- [122] J. Deslippe, M. Dipoppa, D. Prendergast, M. V. O. Moutinho, R. B. Capaz, and S. G. Louie, *Nano Lett.* **9**, 1330 (2009).
- [123] L. Peters, E. Şaşıoğlu, S. Rossen, C. Friedrich, S. Blügel, and M. I. Katsnelson, *Phys. Rev. B* **95**, 155119 (2017).
- [124] L. Peters, E. Şaşıoğlu, I. Mertig, and M. I. Katsnelson, *Phys. Rev. B* **97**, 045121 (2018).
- [125] L. Yang, C.-H. Park, Y.-W. Son, M. L. Cohen, and S. G. Louie, *Phys. Rev. Lett.* **99**, 186801 (2007).
- [126] Y. Miyauchi, M. Oba, and S. Maruyama, *Phys. Rev. B* **74**, 205440 (2006).
- [127] J. Lefebvre and P. Finnie, *Phys. Rev. Lett.* **98**, 167406 (2007).
- [128] J. Deslippe, C. D. Spataru, D. Prendergast, and S. G. Louie, *Nano Lett.* **7**, 1626 (2007).
- [129] F. Wang, D. J. Cho, B. Kessler, J. Deslippe, P. J. Schuck, S. G. Louie, A. Zettl, T. F. Heinz, and Y. R. Shen, *Phys. Rev. Lett.* **99**, 227401 (2007).
- [130] S. Uryu and T. Ando, *Phys. Rev. B* **77**, 205407 (2008).
- [131] H. Kataura, Y. Kumazawa, Y. Maniwa, I. Umezumi, S. Suzuki, Y. Ohtsuka, and Y. Achiba, *Synth. Met.* **103**, 2555 (1999).
- [132] R. Saito, G. Dresselhaus, and M. S. Dresselhaus, *Phys. Rev. B* **61**, 2981 (2000).
- [133] M. J. O'Connell, S. M. Bachilo, C. B. Huffman, V. C. Moore, M. S. Strano, E. H. Haroz, K. L. Rialon, P. J. Boul, W. H. Noon, C. Kittrell, J. Ma, R. H. Hauge, R. B. Weisman, and R. E. Smalley, *Science* **297**, 593 (2002).
- [134] M. Y. Sfeir, F. Wang, L. Huang, C.-C. Chuang, J. Hone, S. P. O'Brien, T. F. Heinz, and L. E. Brus, *Science* **306**, 1540 (2004).
- [135] C. Fantini, A. Jorio, M. Souza, M. S. Strano, M. S. Dresselhaus, and M. A. Pimenta, *Phys. Rev. Lett.* **93**, 147406 (2004).